Tailored P2/O3 phase-dependent electrochemical behavior of Mn-based cathode for sodium-ion batteries

Samriddhi Saxena[a], Hari Narayanan Vasavan[a], Manish Badole[a], Asish Kumar Das[a], Sonia Deswal[b], Pradeep Kumar[b], Sunil Kumar[a, *]

[a] *Department of Metallurgy Engineering and Materials Science, Indian Institute of Technology Indore, Simrol, 453552, India*

[b] *School of Physical Sciences, Indian Institute of Technology Mandi, Mandi, 175005, India*

**E-mail: sunil@iiti.ac.in*

Abstract

The development of mixed structures is increasingly becoming an efficient way to improve the performance of layered oxide cathodes for sodium-ion batteries. Herein, the $Na_{0.8}Mn_{0.6}Ni_{0.3}Cu_{0.1}O_2$ (NMNC) cathodes with varying fractions of P2/O3-type phases are prepared by adjusting the calcination conditions. The Rietveld refinement of X-ray diffraction (XRD) data confirms the increase in O3 phase fraction from 7% to 27% with the increase in calcination temperature from 850 °C to 950 °C. The sample prepared at 850 °C (NMNC-850) exhibits the highest specific capacity (139 mAh g^{-1}, 100 mAh g^{-1}, and 80 mAh g^{-1} at 0.1 C, 1 C, and 4 C, respectively) and best rate performance among all samples in addition to an excellent cyclability with capacity retention of ~ 85% after 100 cycles in 1.5 - 4.2 V range. The increase in the O3 phase fraction leads to a drastic degradation of rate performance. The galvanostatic intermittent titration technique confirms a diffusion coefficient of 5.13×10^{-13} – 5.25×10^{-10} cm^2 s^{-1} in biphasic NMNC-850 sample. Ex-situ XRD studies confirm a reversible P2/O3 → P2/P3 → P2/O3 transformation in NNMC-850 during cycling. The improved electrochemical performance is attributed to the presence of non-identical neighboring phases in suppressing the phase transformations during cycling.

Keywords: Energy storage; Biphasic cathodes; Phase transformation; X-ray diffraction; Diffusion coefficient.

1. Introduction

Energy storage is required to overcome the variations in power supply and demand by providing voltage support and levelling the output fluctuations by renewable energy sources. Among the various available energy storage mechanisms, the electrochemical energy storage systems are dominant owing to their high-efficiency level, fast response time, and low self-discharge [1, 2]. Lithium-ion batteries (LIBs) are a primary example of an electrochemical energy storage system that has been extensively used to meet today's market requirements. However, the uneven and scarce distribution of Li reserves has led to a surge in the manufacturing cost of LIBs and raises sustainability-related issues. This has motivated the scientific community to explore alternative battery technologies [3-5]. Due to the similarity in the working mechanisms of sodium-ion batteries (NIBs) and LIBs, and the relative abundance of Na, NIBs have emerged as a favorable candidate for stationary storage applications [6-9]. The cathode material primarily limits the performance of NIBs, so the development of stable and efficient cathodes is crucial for their commercialization [10-12].

Cathode materials based on layered oxide structures (LOs) (Na_xTMO_2, $x \leq 1$ and TM stands for transition elements Ti, V, Cr, Mn, Fe, Co, Ni, Cu, etc.) have been investigated extensively because of their facile synthesis, tuneable structural properties, and high specific capacity [13-15]. Depending on the number of oxide layers and the location of Na atoms, the LOs are mainly categorized into P2-type, P3-type, and O3-type [16]. Here, the P2-type oxides have adjacent triangular prismatic sites where sodium ions are present, and the O3-type oxides have octahedral geometry around the Na-ions. The larger triangular prismatic sites of P2-type oxides provide wider transport channels to facilitate the diffusion of Na^+, resulting in a better rate capability. In contrast, the higher sodium-ion concentration in O3-type oxides increases their specific capacities [17-19].

Among the transition metal combinations explored in P2 and O3-type layered oxides, Mn-based materials (manganese being an earth-abundant resource) have received the most attention. The Na-Mn-O system of cathodes is known to have specific capacities upwards of 190 mAh g^{-1} [13, 20]. However, due to lower reduction potentials of Mn^{3+}/Mn^{4+} redox couple (typically in the range of 2 – 3 V), these materials exhibit low open circuit voltages (~3 V). Moreover, the presence of Jahn-Teller active Mn^{3+} induces distortions and phase transformations at lower voltages leading to poor cyclic performance of these cathodes [21, 22]. Elements such as Ni and Cu have been substituted for Mn in the Na_xMnO_2-based cathodes to minimize the structural distortions during cycling. Although the 2+ oxidation states of Ni and Cu ions force Mn^{3+} to Mn^{4+} transformations during synthesis, the reduction in specific capacity is compensated by Ni^{2+}/Ni^{4+} redox couple, which is a 2-electrons transfer in contrast to the Mn^{3+}/Mn^{4+} redox couple with just one-electron transfer. Other properties of the material, such as moisture stability, cyclability, nominal voltage, etc., are also reported to be enhanced by the inclusion of Cu ions [23-25]. Recently, certain compositions in the $Na_x(Mn\text{-}Ni\text{-}Cu)O_2$ system have exhibited a specific capacity of ~90 mAh g^{-1} with a nominal voltage of ~3.4 V and excellent capacity retention of ~ 80% after 200 cycles at 0.1 C [24, 26, 27].

However, to improve the practical applicability of $Na_x(Mn\text{-}Ni\text{-}Cu)O_2$, cyclability and rate performance should be enhanced further. One typical method to solve this problem includes lowering the cut-off voltage for charging, which prevents the phase transitions from occurring at high voltages at the expense of the specific capacity [28]. A minor inert-ion substitution (such as Mg [29, 30], Li [31, 32], Zn [33, 34], etc.) is another strategy for structural stabilization during the charge-discharge cycle. This helps in subduing the irreversible phase transitions and Na-vacancy ordering with improved air stability [35, 36]. Recently, the intergrowth of multi-phase structures has emerged as an alternative strategy to improve electrochemical performance without compromising on specific capacity [37-39]. The synergy between P2 and

O3 phases enhances the electrochemical performance of the biphasic cathodes compared to the single-phase cathodes [40-42]. The composite structures can be tailored by employing numerous strategies, such as tuning different stoichiometric ratios of raw materials, ions substitution, and varying synthesis parameters (calcination temperature, reaction time, sodium content, etc.) [35, 43, 44]. Presently, substituting metal cations in LOs is a popular method to prepare composite layered oxides [45]. For instance, Li^+/Ti^{4+} co-substituted P2/O3-$Na_{0.67}Li_{0.11}Fe_{0.36}Mn_{0.36}Ti_{0.17}O_2$ showed excellent cyclability in the voltage range of 2.0- 4.2 V [41]. A P2/O3-$Na_{0.8}Mn_{0.55}Ni_{0.25}Fe_{0.1}Ti_{0.1}O_2$ cathode material was prepared by adjusting the ratio of Ni and Mn, which showed improved rate capability than that of the original P2 and O3 phases [39]. In addition to the composite structure, the variable stoichiometric ratios of the constituent elements also contribute to the electrochemical enhancement of the ion-substituted biphase materials. However, the independent impact of the biphase structure on the electrochemical performance is yet to be elucidated.

Herein, biphasic $Na_{0.8}Mn_{0.6}Ni_{0.3}Cu_{0.1}O_2$ (NMNC-T) materials with varying P2/O3 phase fractions are successfully obtained by tuning the calcination temperatures in 800 to 950 °C range, and their impact on the electrochemical behavior is systematically investigated. To the best of our knowledge, the $Na_{0.8}Mn_{0.6}Ni_{0.3}Cu_{0.1}O_2$ composition with varied P2/O3 phase fractions is extensively investigated as a potential cathode material for sodium-ion batteries for the first time. This study confirms that the synergistic effects of the composite structure improve the specific capacity and cyclability by reducing the lattice strain during the charge-discharge process via the interlocking effect of the phase boundaries; however, the increase in the O3 phase fraction has a determinantal effect on the C-rate performance. Unlike many other single-phase materials in the Na-Ni-Mn system, biphasic $Na_{0.8}Mn_{0.6}Ni_{0.3}Cu_{0.1}O_2$ composition exhibits much-improved cyclability even in the Jahn-Teller active 1.5 – 4.2 V range.

2. Experimental

2.1. Synthesis

A simple sol-gel technique was used to synthesize the biphasic $Na_{0.8}Mn_{0.6}Ni_{0.3}Cu_{0.1}O_2$ materials. Stoichiometric amounts of manganese (II) acetate tetrahydrate, nickel acetate tetrahydrate, copper (II) nitrate trihydrate, and sodium carbonate were mixed in deionized water followed by stirring for 8 h. To this, citric acid and ethylene glycol were added in appropriate amounts and stirred for another 12 h to obtain a uniform solution. This solution was heated at about 80 °C to form a gel. The dried gel was ground before heat-treating at 550 °C for 12 h. The resultant powders were ground and calcined in air at various temperatures in the 800 - 950 °C range for 12 h in air to get the final product. These calcined $Na_{0.8}Mn_{0.6}Ni_{0.3}Cu_{0.1}O_2$ powders were labeled as NMNC-T; here, T denotes the calcination temperature = 800 °C, 850 °C, 900 °C, and 950 °C.

2.2. Characterization

An Empyrean, Malvern Pananalytical diffractometer with Cu-K_α radiation source was used to perform powder X-ray diffraction (XRD) within the 2θ range of 10°- 80° at room temperature. *TOPAS Academic* (version 6) software package was used to perform Rietveld refinement of the XRD data to calculate the crystallographic parameters of all samples [46]. The morphology and elemental distribution in powder samples were investigated using a field emission scanning electron microscope (SEM) (model JEOL-7610) equipped with energy-dispersive X-ray spectroscopy (EDS). A Thermofisher Scientific (Naxsa base) having a 1486.6 eV (Al Kα) X-ray source was used to take X-ray photoelectron spectroscopy (XPS) measurements to ascertain the oxidation states of various elements present in NMNC samples.

For electrochemical studies, CR-2032 coin cells were fabricated using Na metal as the counter electrode, Whatman GF/D as the separator, and 1 M $NaClO_4$ in ethylene carbonate – propylene carbonate (EC-PC) in the volume ratio of 1:1 as the electrolyte. The cathode was prepared by mixing 80 wt.% active material, 10 wt.% Ketjen black, and 10 wt.% PVDF binder in N-Methylpyrrolidone (NMP) solvent. The slurry was then coated on an Al current collector, dried at 120 °C for 8 h in a vacuum oven, and punched into 16 mm disks. The active material mass loading was ~ 3-4 mg $cm^{-2,}$ and an apparent active mass density of ~ 1.5-2.0 g cm^{-3}. A Keithley source meter unit (Model 2450-EC) was employed to perform cyclic voltammetry (CV) on the coin cell between 1.5 V and 4.2 V with a scan rate of 0.1 mV s^{-1}. A Landt battery testing system (LANHE CT, 2001A) was used for Galvanometric charge-discharge (GCD) tests on the coin cell within 1.5 V – 4.2 V. The rate performance of the cathode was evaluated at 0.1 C, 0.2 C, 1 C, 2 C, and 4 C, while the cyclability tests were performed at 0.2 C for 100 cycles between 1.5 V and 4.2 V. Calculation of C-rates was done by assuming a specific capacity of 170 mAh g^{-1}. The galvanostatic intermittent titration technique (GITT) was used to calculate the sodium-ion diffusion coefficient of the half-cells using a Neware Battery Tester (Model no.CT-4008T).

3. Results and discussion

3.1. XRD

The XRD patterns of the NMMC-T samples calcined at various temperatures (T = 800 °C - 950 °C) are depicted in Fig. 1. Preliminary analysis of the XRD data shows the existence of a biphasic system consisting of P2 and O3 phases for NMMC-850, NMMC-900, and NMMC-950 samples, whereas, additional peaks belonging to P3 and other impurity phases are visible in the pattern for the sample NNMC-800. Accordingly, the NNMC-800 sample was not characterized further in this work. It is clear from Fig. 1 that with the increase in calcination temperature, the peak intensity of the O3 phase shows a continuous upward trend indicating an increase in the O3 phase fraction, which is reported to be more stable at higher temperatures [47]. The crystal structure and P2/O3 phase fractions for the as-prepared NMNC samples were ascertained by performing Rietveld refinement of the powder XRD data. The refinement profiles for the samples (T = 850 °C, 900 °C, and 950 °C) and their corresponding phase fractions are shown in Fig. 2 (a-c) and Fig. 2(d), respectively. The calculated structural parameters are given in Table 1.

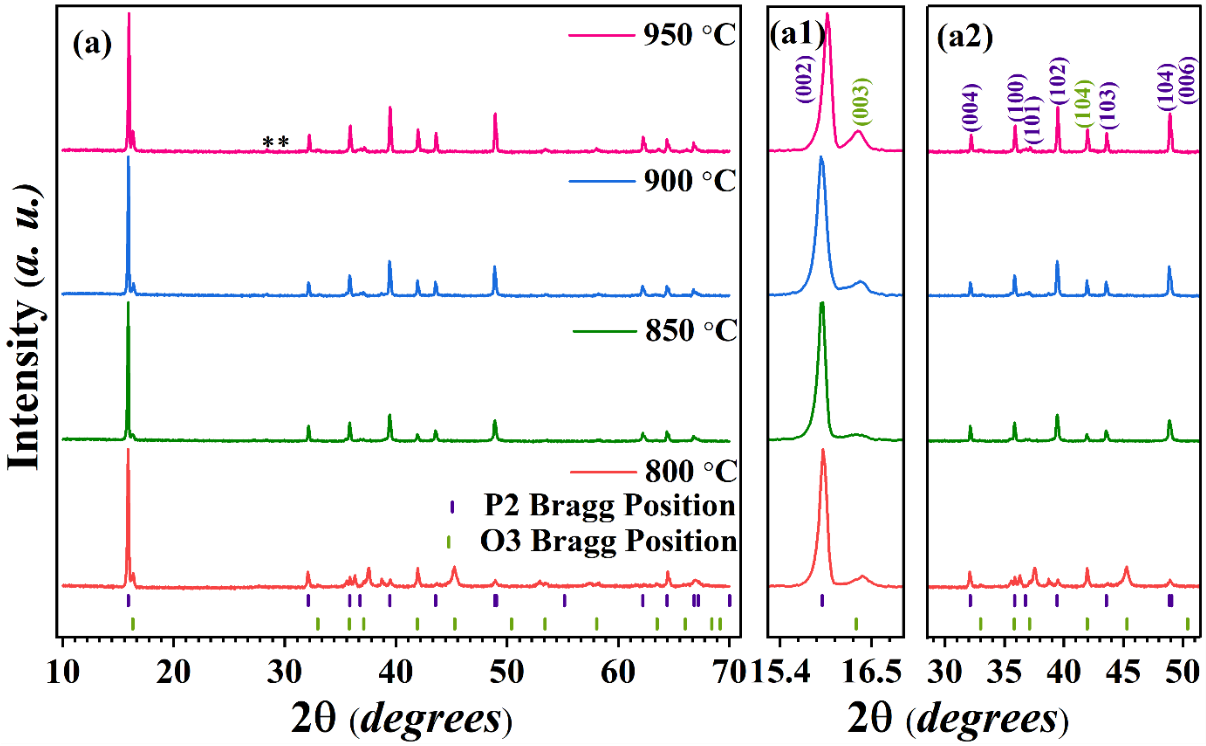

Fig. 1. (a) XRD patterns showing the simultaneous existence of P2 and O3 phases and their phase evolution with calcination temperature in NMNC–T (T = 800 °C, 850 °C, 900 °C, 950 °C). Magnified view of (a1) (002) peak of P2 phase and (003) peak of O3 phase, (a2) (004), (100), (101), (102), (103), (104), (006) of P2 phase and (104) of O3 phase.

The refinement of the XRD data confirms that all three samples crystallize in a biphasic P2 ($P6_3/mmc$ space group) and O3-type ($R\bar{3}m$ space group) structure with hexagonal symmetries. The ordering of Na-ion vacancies induces superlattice reflections which can be observed as two minor peaks at ~ 27.2° and 28.3° (marked by * in Fig. 1) in the XRD patterns [48-50]. The various crystallographic parameters of all samples calculated from the Rietveld refinement of the XRD data are depicted in Tables S1-S3 (Supplementary Material).

VESTA software was employed to visualize the XRD refinement data, and it showed a decrease in the volume of Na-O_6 prisms with the increase in calcination temperature. The *c*-lattice parameter of the P2 phases of the NMNC-T sample decreases marginally on the rise in T, whereas the lattice parameter *a* increases (Table 1). The rectangular bottleneck area for the sodium ion diffusion in the P2 phase is found to decrease from ~ 10.2609 Å^2 to ~ 10.1537 Å^2 with an increase in temperature from 850 °C to 950 °C (Fig. 2 (e)). Moreover, the O3 phase fraction increases from ~ 7% for NMNC–850 to ~ 13 % for NMNC–900 and then to ~ 27% for NMNC–950 samples. It is well-known that Na-ion diffusion in O3-type layered oxides is sluggish compared to their P2-type counterparts as Na-ion moves across adjacent octahedra via a narrower triangular face bottleneck in the former (Fig. 2(f)). Consequently, the Na-ions migration in the NMNC-850 sample is expected to be better than the other samples due to a higher fraction of the P2 phase.

Sample	***Phase***	***a* (Å)**	***c* (Å)**	***V* (Å^3)**	**R_{exp}, R_{wp}, R_p, *GOF***
T = 850 °C	P2	2.89169 ± 0.00007	11.1374 ± 0.0006	80.653 ± 0.006	2.23, 3.38, 2.44, 1.51
	O3	2.9308 ± 0.0005	16.258 ± 0.005	120.94 ± 0.05	
T = 900 °C	P2	2.89323 ± 0.00006	11.1356 ± 0.0005	80.798 ± 0.005	3.25, 3.25, 2.44, 1.49
	O3	2.9343 ± 0.0002	16.232 ± 0.002	121.04 ± 0.02	
	P2	2.89383 ± 0.00005	11.1340 ± 0.0004	80.784 ± 0.005	2.21, 2.96, 2.30, 1.33

T = 950 °C	O3	2.9272 ± 0.0001	16.327 ± 0.001	121.17 ± 0.01	

Table 1 Lattice parameters of P2/O3 NMNC – T samples obtained from Rietveld refinement of XRD data.

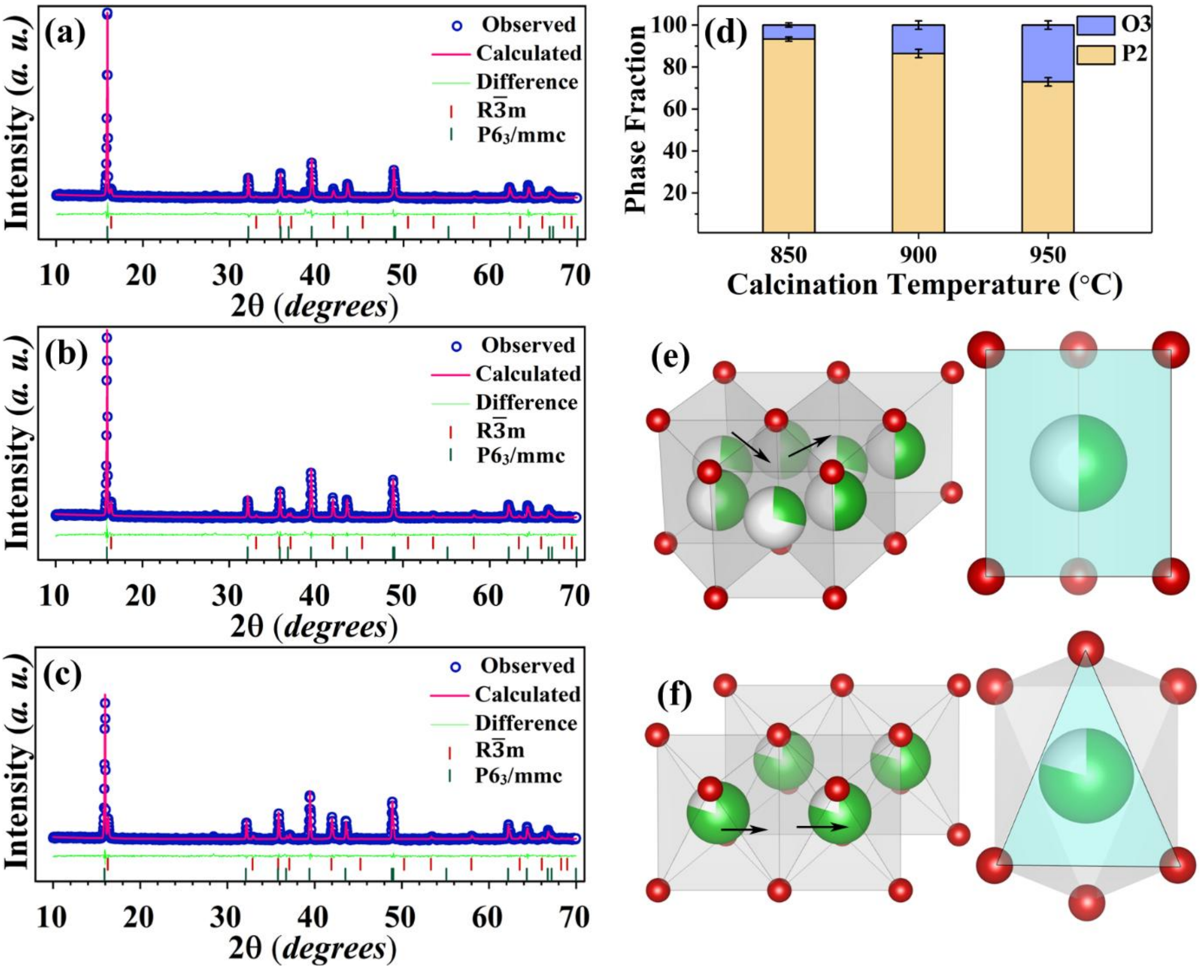

Fig. 2. Rietveld refinement profiles of XRD data for NMNC samples calcined at (a) T = 850 °C, (b) T = 900 °C, and (c) T = 950 °C. (d) Schematic of phase fractions at different temperatures. Na^+ migration pathways (represented by arrows) in (e) prisms of the P2 phase through a rectangular (highlighted in cyan color) box directly entering the adjacent prisms and (f) octahedron of the O3 phase through a triangular face (highlighted in cyan color) in a tetrahedron between adjacent two octahedra.

3.2. SEM

The SEM micrographs of NMNC-T samples are shown in Fig. 3, along with the representative elemental map for NMNC-850. The images show that the hexagonally shaped particles of NMNC-850 have an average particle size of 2.4 ± 0.8 μm, lesser than NMNC-900 and NMNC-950 (with an average particle size of 2.9 ± 0.7 and 4.6 ± 1.3 μm, respectively), which could be attributed to the difference in calcination temperature. The comparatively lower surface energy of the (*00l*) surface in contrast to (*h00*), (*0k0*), and (*hk0*) surfaces can be used to explain the hexagonal plate-like morphology of the NMNC-T samples [19, 51, 52]. Therefore, the (*00l*) surface will dominate the equilibrium shape of NMNC-T crystals. The EDS mapping of the NMNC-850 sample (Fig. 3(d1-5)) confirms that the distribution of Na, Mn, Ni, Cu, and O is uniform throughout the sample without any evident segregation. Fig. S4 (a-e) shows the magnified SEM images of NMNC-T samples. It can be seen that the surface of all particles is smooth, and particles are agglomerated. This confirms that the chelating agent does not affect the surface smoothness of the individual particles.

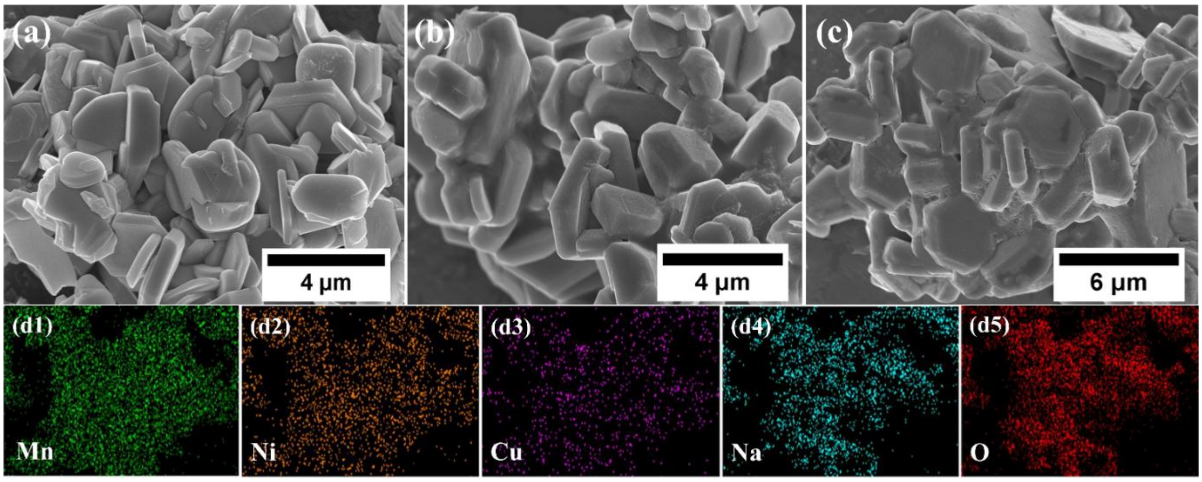

Fig. 3. SEM images of (a) NMNC-850, (b) NMNC-900 (c) NMNC-950. (d1)-(d5) EDS spectra of NMNC-850 indicating uniform distribution of constituent elements.

3.3. XPS

Oxidation states of the constituent transition metals of NMNC-T samples were confirmed by X-ray photoelectron spectroscopy. Fig. 4. depicts the XPS spectra of Cu 2p, Mn 2p, and Ni 2p from different samples. The Ni 2p spectrum shows four characteristic peaks that can be assigned to Ni $2p_{3/2}$ (~ 854 eV), Ni $2p_{1/2}$ (~ 872 eV), and their corresponding satellite peaks. This suggests a 2+ oxidation state for Ni-ions in the materials [27, 53, 54]. In the Cu 2p spectra, the two peaks at ~ 932 eV ($2p_{3/2}$) and ~ 952 eV ($2p_{1/2}$) confirm the presence of Cu^{2+} [27, 53, 54]. The two peaks at ~ 641 and ~ 652 eV in the Mn 2p spectra are assigned to $2p_{1/2}$ and $2p_{3/2}$, respectively, signifying the existence of Mn as Mn^{4+} in the materials [27, 53, 54]. The XPS data suggests the independence of oxidation states of the constituent elements with temperature in the cathode materials.

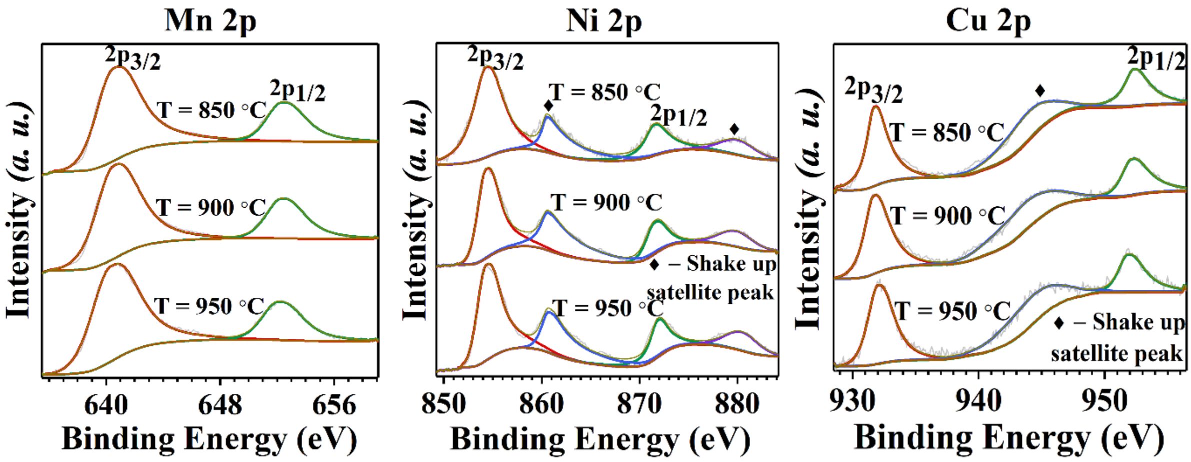

Fig. 4. XPS spectra of NMNC–T samples (T = 850 °C, 900 °C, and 950 °C).

3.4. CV

Cyclic voltammetry (CV) tests were performed on the prepared cathode materials to study their redox activity. Fig. 5 shows the CV profile of NMNC-850 half-cells between a voltage window of 1.5 - 4.2 V at a scan rate of 0.1 mV s^{-1}, and the cyclic voltammograms of NMNC-900 and NMNC-950 are provided in Fig. S1. During oxidation-reduction cycle, the series of oxidation/reduction peaks between 3.0 and 3.9 V can be ascribed to the Ni^{2+}/Ni^{4+} redox reaction and the Na^{+}/vacancy ordering mechanism [55, 56]. The peak at about 3.9 V in the CV curves indicates the activation of the Cu^{2+}/Cu^{3+} redox pair [24-26]. Although Mn is in an electrochemically inactive 4+ oxidation state in the as-prepared material, a small peak in the CV plot suggests minor Mn redox activity in the 1.5 - 2.0 V range [57-59]. This can be attributed to the Na-ion insertion process below the open circuit voltage against Na/Na^{+}, which triggers the reduction of some Mn^{4+} into Mn^{3+} [59-61]. The similarity in the CV curves of the second and third cycles for all cathodes indicates that all redox processes are reversible.

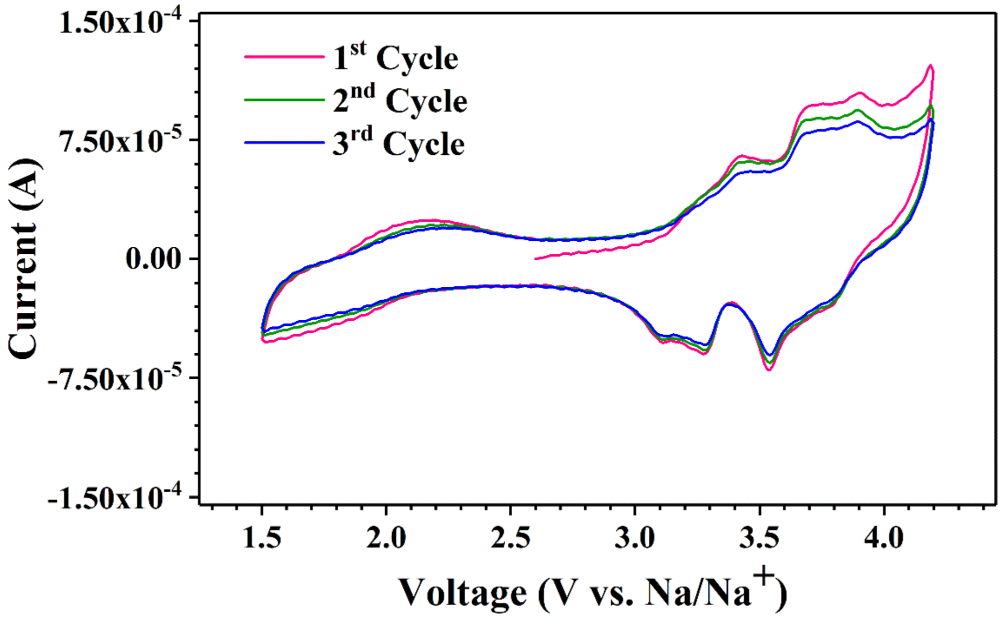

Fig. 5. Cyclic voltammogram of NMNC-850 sample at a scan rate of 0.1 mV s^{-1}.

3.5. GCD

To further probe the influence of different phase compositions on the electrochemical performance, the cathodes were tested in a half-cell configuration between 1.5 V to 4.2 V, and the results are shown in Fig. 6. The galvanostatic charge-discharge (GCD) voltage profiles of the NMNC-T cathodes at different C rates are given in Fig. 6(a)-(d) and Fig. S5-S7 depicts the first galvanostatic charge/discharge cycles of NMNC–T samples at 0.1 C in 1.5-4.2 V.

The samples calcined at 850 °C, 900 °C, and 950 °C deliver specific capacities of ~ 139 mAh g^{-1}, 119 mAh g^{-1}, and 107 mAh g^{-1} at 0.1 C, respectively. The NMNC-850 sample shows a specific capacity of ~ 116 mAh g^{-1} and 100 mAh g^{-1} at 0.2 C and 1 C, respectively (Fig. 6. (d)).

Even at 4 C, the sample calcined at 850 °C retains a capacity of 80 mAh g^{-1}, while the other samples show almost negligible capacities. These phenomena demonstrate the higher structural reversibility of NMNC-850. This is attributed to the higher percentage of the P2 phase in the sample, with a larger conduction pathway, as indicated in the XRD section. This allows the Na-ions to move swiftly during charge-discharge, allowing for greater and more efficient Na-ion extraction, resulting in better rate performance. Although increasing the O3 phase percentage with temperature is expected to result in high specific capacity, the agglomeration of particles at higher treatment temperatures could hinder the Na-ion extraction and lead to a reduction in specific capacity at high C rates. In Fig. 6, the Ni^{2+}/Ni^{3+} and Ni^{3+}/Ni^{4+} redox couples result in plateaus above 3.0 V, while the Cu^{2+}/Cu^{3+} redox couple gives rise to the plateau above 3.75 V [24, 62, 63].

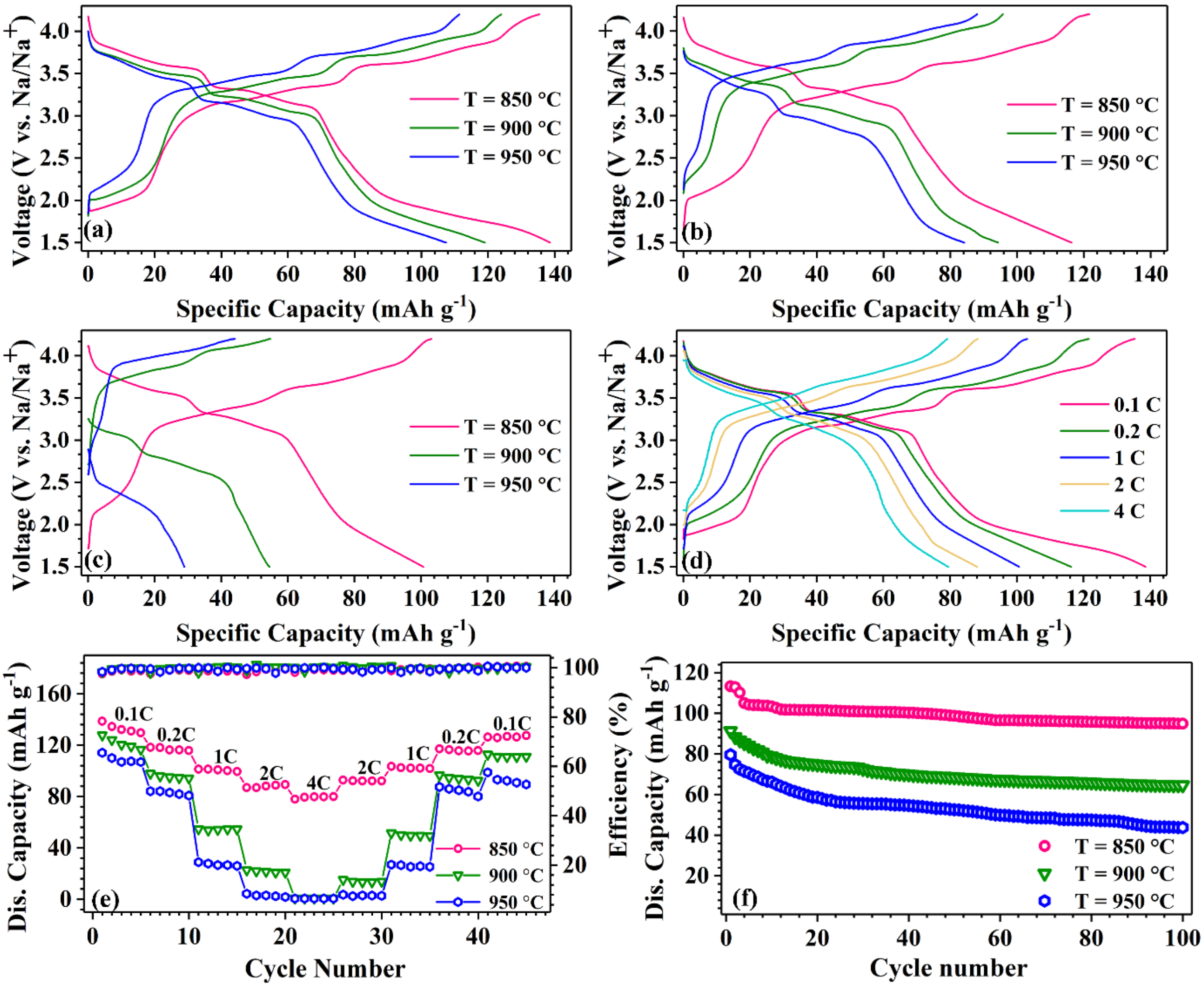

Fig. 6. Galvanostatic charge-discharge curves of NMNC–T samples (T = 850 °C, 900 °C, and 950 °C) at (a) 0.1 C, (b) 0.2 C, (c) 1 C, and (d) P2/O3 NMNC–850 sample at different C rates. (e) Rate performance and Coulombic efficiency of the NMNC–T samples. (f) Cycle performance of P2/O3 NMNC–T at 0.2 C.

The cycling performance of NMNC–T cathodes was evaluated at a 0.2 C rate between 1.5 V and 4.2 V, as shown in Fig. 6. (f). After 100 cycles, NMNC-850 has the most consistent cycling performance, with a capacity retention of ~ 85% of the initial capacity. In contrast, the capacity retention of NMNC-900 and NMNC-950 is only ~ 70% and ~ 54%, respectively. Table 2 summarizes the reported capacity retention of various cathodes for sodium-ion batteries in a wide voltage window [43, 64]. It is evident that the single-phase cathode materials have limited capacity retention (≤ 50 cycles). Even the materials with pillar ions, such as Mg, Fe, Li, etc., which are meant to support the structure and alleviate the adverse effects of phase transformations, have shown only moderate improvement in cyclability. The coexistence of P2 and O3 phases in the $Na_{0.8}Mn_{0.6}Ni_{0.3}Cu_{0.1}O_2$ structure hinders the phase transformation induced by Jahn-Teller active Mn^{3+}. This allows us to utilize the voltage range of 1.5 to 2.0 V for electrochemical studies, which was forbidden, as reported previously [65-70].

Material	***Phase***	***Voltage Range (V vs. Na/Na+)***	***Current rate***	***Capacity Retention***	***Ref.***
$Na_{0.67}Mn_{0.8}Ni_{0.1}Mg_{0.1}O_2$	P2	1.5 - 4.2 V	0.1 C	79% 50 cycles	[67]
$Na_{0.67}Fe_{0.20}Ni_{0.15}Mn_{0.65}O_2$	P2	1.5 - 4.3 V	0.1 C	55% 30 cycles	[66]
$Na_{0.67}Mn_{0.6}Ni_{0.2}Cu_{0.1}Mg_{0.1}O_2$	P2	1.5 - 4.5 V	0.2 C	75% 24 cycles	[70]

$NaLi_{0.1}Ni_{0.35}Mn_{0.55}O_2$	O3	1.5 - 4.3 V	0.1 C	83% 30 cycles	[68]
$NaNi_{0.3}2Fe_{0.13}Co_{0.15}Mn_{0.40}O_2$	O3	1.5 - 4.3 V	0.1 C	85% 50 cycles	[65]
$NaNi_{0.65}Co_{0.08}Mn_{0.27}O_2$	O3	1.5 - 4.1 V	0.5 C	77% 50 cycles	[69]
$Na_{0.67}Li_{0.15}Ni_{0.18}Mg_{0.02}Mn_{0.8}O_2$	P2/O3	1.5 - 4.2 V	0.1 C	70%, 100 cycles	[71]
$Na_{0.67}Li_{0.2}Fe_{0.2}Mn_{0.6}O_2$	P2/O3	1.5 - 4.5 V	0.1C	85%, 60 cycles	[40]
$Na_{0.73}Ni_{0.4}Mn_{0.4}Ti_{0.2}O_2$	P2/O3	1.5 - 4.4 V	0.5 C	81%, 50 cycles	[72]
$Na_{2/3}Li_{0.18}Fe_{0.2}Mn_{0.8}O_2$	P2/O3	1.5 - 4.2 V	0.1 C	69%, 100 cycles	[73]
$Na_{0.67}Ni_{0.4}Co_{0.2}Mn_{0.4}O_2$	P2/O3	1.5 - 4.2 V	0.1 C	81%, 100 cycles	[74]
$Na_{0.8}Mn_{0.6}Ni_{0.3}Cu_{0.1}O_2$	P2/O3	1.5 - 4.2 V	0.2 C	**85%** **100 cycles**	This work

Table 2 Comparison of capacity retention in a wide voltage range of various cathode materials for sodium-ion batteries

3.6. GITT

The diffusion kinetics of Na^+ in the biphasic NMNC is investigated by employing the galvanostatic intermittent titration technique (GITT) in the 1.5 - 4.2 V voltage range, and the results are shown in Fig. 7. and Figs. S2-S3. In this method, the cell is subjected to a galvanostatic process for a definite time interval followed by a rest period. Here, GITT was used on the cell after cycling it two times. A constant current pulse was applied for 10 minutes, followed by 30 minutes relaxation of the cell to reach a quasi-equilibrium state.

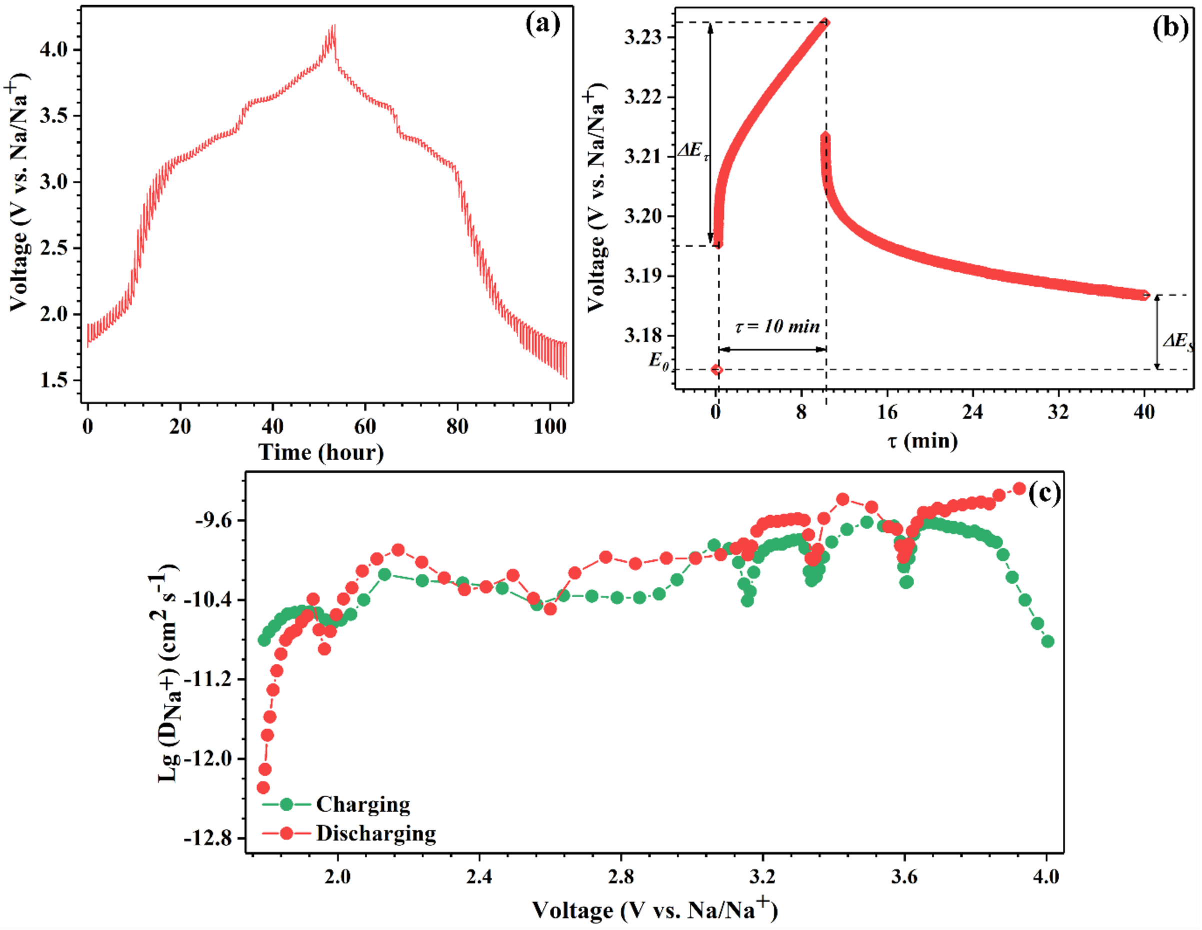

Fig. 7. (a) GITT profile of NMNC-850 electrode. (b) A single titration unit in GITT. (c) Diffusion coefficient of Na$^+$ at different stages during charge-discharge.

The diffusion of Na-ions into the cathode material is assumed to obey Fick's first law and can be calculated using the following Eq. 1. [75]

$$D_{Na^+} = \frac{4}{\pi\tau}\left(\frac{m_B V_m}{M_B S}\right)^2 \left(\frac{\Delta E_S}{\Delta E_\tau}\right)^2 \qquad (t \ll L^2 / D) \qquad (1)$$

Here, τ corresponds to the time of a single constant current pulse, m_B represents the mass of active material, V_m and M_B represent the molar volume and molar mass of cathode material, and S is the active surface area of the electrode. ΔE_S and ΔE_τ denote the change of the steadystate voltage and the voltage change during the constant current pulse, respectively. Na^+ diffusion coefficients (D_{Na}^+) of NMNC-850 are in the range of 5.13×10^{-13} – 5.25×10^{-10} cm^2 s^{-1}, while the D_{Na}^+ of NMNC-900 and NMNC-950 ranges between 1.17×10^{-13} – 6.45×10^{-11} cm^2 s^{-1} and 9.43×10^{-14} – 3.70×10^{-11} cm^2 s^{-1}, respectively. Comparing the D_{Na}^+ of the cathodes, NMNC-850 has slightly higher diffusion coefficients than the other two samples, which could be attributed to the larger Na^+ migration channel in NMNC-850, as confirmed by the XRD analysis. It can be observed that the diffusion coefficient undergoes a drop at higher voltages signifying that the electrochemical kinetics is relatively slow when the structure has a smaller number of Na^+ cations [76]. Similarly, during discharging to lower voltages, when the cathode is saturated with Na^+, the diffusion coefficient drops rapidly, signifying poor diffusion kinetics. Further, electrochemical impedance spectroscopy (EIS) was carried out on half-cells employing cathode materials calcined at different temperatures. Fig. S9 shows the room temperature Nyquist plots for all cells and the equivalent circuit (inset) used to fit the impedance data. The overall resistance of the NMNC-850 cell is ~ 183 Ω, which is much lower when compared to NMNC-900 (~ 646 Ω) and NMNC-950 (~ 1850 Ω) cells. These results confirm that the relatively higher diffusion coefficient of NMNC-850 facilitates sodium ion conduction through the material, leading to improved electrochemical performance at higher C rates.

3.7. Ex-situ XRD

Ex-situ XRD experiments on the NMNC-850 and NMNC-900 samples at various states of charges (charged and discharged to different voltages) were conducted to study the change in structural parameters during cycling, and the results are shown in Fig. 8 and Fig. S8, respectively. During charging, the (002) and (004) peaks of P2 in the biphase material gradually shift towards a lower 2θ (Fig. 8(a)). This indicates an increment in the repulsive forces among TMO_2 layers, which increases the interlayer spacing with the Na^+ extraction [33, 77, 78].

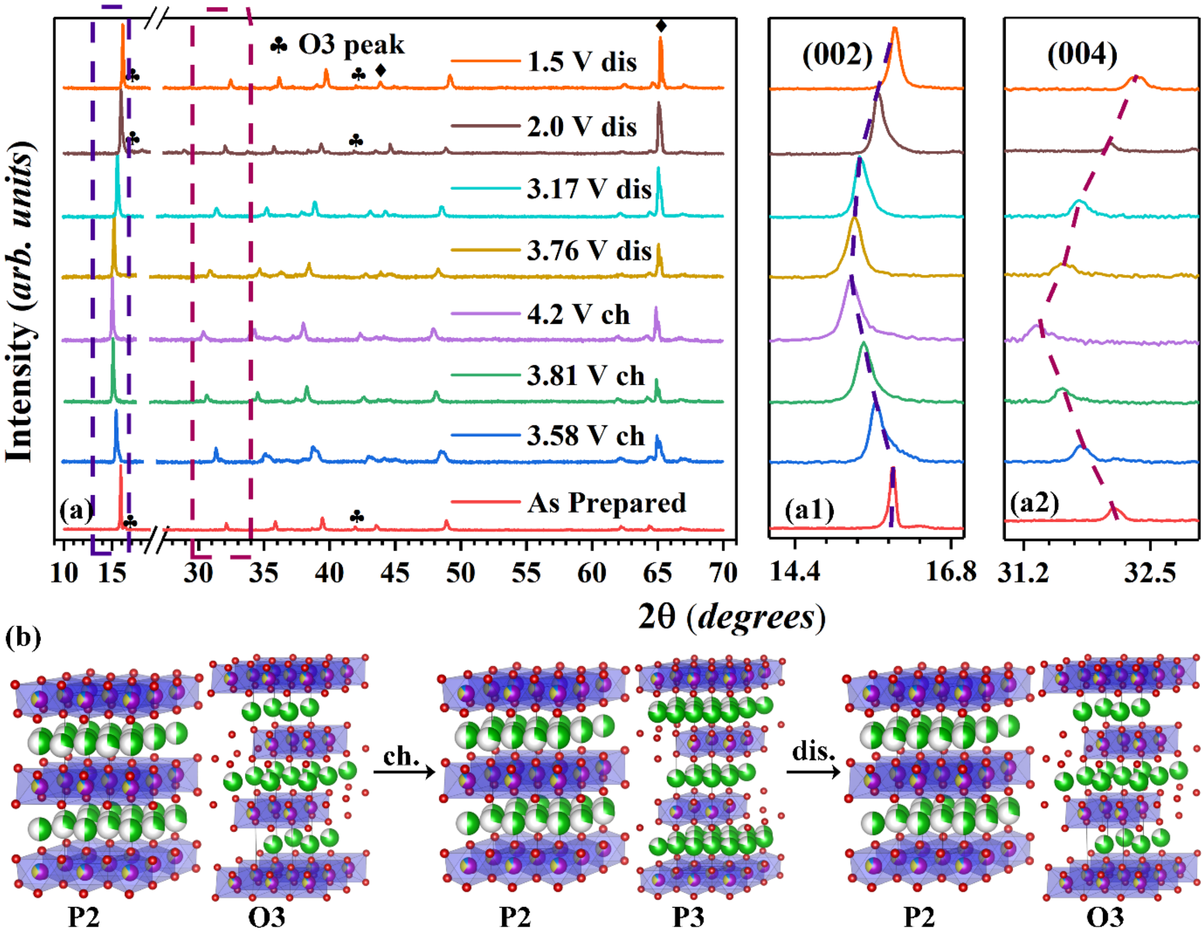

Fig. 8. Ex-situ XRD patterns of NMNC-850 sample at different states of charge between 1.5 and 4.2 V during charging (ch) and discharging (dis) at 0.1 C and (a1), (a2) showing the enlarged view of patterns of P2-(002) and P2-(004) peaks. The peaks denoted by ♣ represent O3 characteristic peaks returning to their initial state during discharge. The Al peaks (denoted by ◆) belong to the Al current collector. (b) Corresponding crystal structure evolution of the material during charge-discharge.

During charging, the characteristic (003) and (104) diffraction peaks of the O3 phase disappear, indicating the transformation of the O3 phase to the P3 phase. The sample discharged to 1.5 V has a certain offset angle from the as-prepared sample. This is due to the higher amount of Na in the 1.5 V discharged sample, increasing the screening effect on oxygen atoms of TMO_2 layers and causing the *c*-lattice parameter to shrink. It is important to note that the Na^+

extraction has only caused a shift in the position of the (002) peak of the P2 phase and indicates the suppression of the destructive phase transition from P2 to O2. The ex-situ XRD data suggests that the structure of NMNC-850 is converted in a reversible process to P2/O3→P2/P3 and then P2/P3→P2/O3 (Fig. 8(b)), indicating remarkable structural stability. During the intercalation and deintercalation of Na^+, each structure in NMNC-850 is expected to undergo P- to O-type or O- to P-type transformations by the gliding of TMO_2 layers along the *c*-axis. A different phase in the adjacent structure inhibits this gliding of TMO_2 layers. This synergistic interaction between the different phases produces an *interlocking effect*, which reduces the lattice mismatch and creates a structural constraint effect. Therefore, the gliding of transition metal slabs is mitigated, facilitating the improvement in the electrochemical performance [41, 79].

4. Conclusions

In summary, P2/O3 $Na_{0.8}Mn_{0.6}Ni_{0.3}Cu_{0.1}O_2$ biphase cathode materials were synthesized with different phase fractions by varying the calcination temperature (800 to 950 °C) to study the effect on structural and electrochemical properties. The XRD patterns confirmed the coexistence of P2 and O3 phases in all samples. Rietveld refinement of XRD data showed that the $Na_{0.8}Mn_{0.6}Ni_{0.3}Cu_{0.1}O_2$ sample calcined at 850 °C (NMNC-850) has the P2:O3 phase fraction of 0.93:0.07 and the largest bottleneck area for facile sodium-ion conduction. The larger Na^+ migration channel in NMNC-850 was confirmed by a higher Na^+ diffusion coefficient. NMNC-850 showed a specific capacity of 139 mAh g^{-1} at a 0.1 C rate between 1.5 to 4.2 V. The sample also showed a superior rate performance with a discharge capacity of ~ 116 and 100 mAh g^{-1} at 0.2 C and 1 C, respectively. Interestingly, at a high C rate of 4 C, this sample retained a specific capacity of 80 mAh g^{-1}, whereas only a negligible capacity is observed for NMNC-900 and NMNC-950 samples. The synergistic interaction between different phases during the charge-discharge process hinders the detrimental effects of Jahn-

Teller active Mn^{3+}, and the NMNC-850 sample showed a remarkable improvement in cyclability with 85% specific capacity retention even after 100 cycles. These results signify the influence of calcination temperature on phase fraction in P2/O3 biphasic structures, which could be a practical approach to improving the electrochemical performance of cathodes in Na-ion batteries.

CRediT authorship contribution statement

Samriddhi Saxena: Designed the research, powder preparation, fabrication of half-cells, and electrochemical experiments, formal analysis, Writing – original draft; **Hari Narayanan Vasavan:** Formal analysis of XRD data, Writing – review & editing; **Manish Badole:** XRD & SEM measurements; **Asish Kumar Das:** Writing – review & editing; **Sonia Deswal:** performed XPS measurements; **Pradeep Kumar:** XPS analysis; **Sunil Kumar:** Funding acquisition, conceptualization, supervision, conceived the idea and supervised the work; wrote the manuscript with input from all authors.

Declaration of competing interest

The authors declare no competing financial interest.

Acknowledgements

SK thanks the Science and Engineering Research Board (SERB), Govt. of India, for the financial support (grant number: CRG/2021/005548).

References

[1] B. Dunn, H. Kamath, J.-M. Tarascon, Electrical Energy Storage for the Grid: A Battery of Choices, Science 334(6058) (2011) 928-935. https://doi.org/10.1126/science.1212741.

[2] H. Ibrahim, A. Ilinca, J. Perron, Energy storage systems—Characteristics and comparisons, Renewable Sustainable Energy Rev. 12(5) (2008) 1221-1250. https://doi.org/10.1016/j.rser.2007.01.023.

[3] J.-Y. Hwang, S.-T. Myung, Y.-K. Sun, Sodium-ion batteries: present and future, Chem. Soc. Rev. 46(12) (2017) 3529-3614. https://doi.org/10.1039/C6CS00776G.

[4] D. Larcher, J.M. Tarascon, Towards greener and more sustainable batteries for electrical energy storage, Nat. Chem 7(1) (2015) 19-29. https://doi.org/10.1038/nchem.2085.

[5] N. Yabuuchi, K. Kubota, M. Dahbi, S. Komaba, Research Development on Sodium-Ion Batteries, Chem. Rev. 114(23) (2014) 11636-11682. https://doi.org/10.1021/cr500192f.

[6] V. Palomares, P. Serras, I. Villaluenga, K.B. Hueso, J. Carretero-González, T. Rojo, Na-ion batteries, recent advances and present challenges to become low cost energy storage systems, Energy Environ. Sci. 5(3) (2012) 5884-5901. https://doi.org/10.1039/C2EE02781J.

[7] K.M. Abraham, How Comparable Are Sodium-Ion Batteries to Lithium-Ion Counterparts?, ACS Energy Lett. 5(11) (2020) 3544-3547. https://doi.org/10.1021/acsenergylett.0c02181.

[8] J.F. Peters, A. Peña Cruz, M. Weil, Exploring the Economic Potential of Sodium-Ion Batteries, Batteries 5(1) (2019) 10. https://doi.org/10.3390/batteries5010010.

[9] C. Vaalma, D. Buchholz, M. Weil, S. Passerini, A cost and resource analysis of sodium-ion batteries, Nat. Rev. Mater. 3(4) (2018) 18013. https://doi.org/10.1038/natrevmats.2018.13.

[10] E. Goikolea, V. Palomares, S. Wang, I.R. de Larramendi, X. Guo, G. Wang, T. Rojo, Na-Ion Batteries—Approaching Old and New Challenges, Adv. Energy Mater. 10(44) (2020) 2002055. https://doi.org/10.1002/aenm.202002055.

[11] W. Zhang, J. Lu, Z. Guo, Challenges and future perspectives on sodium and potassium ion batteries for grid-scale energy storage, Mater. Today 50 (2021) 400-417. https://doi.org/10.1016/j.mattod.2021.03.015.

[12] R. Usiskin, Y. Lu, J. Popovic, M. Law, P. Balaya, Y.-S. Hu, J. Maier, Fundamentals, status and promise of sodium-based batteries, Nat. Rev. Mater. 6(11) (2021) 1020-1035. https://doi.org/10.1038/s41578-021-00324-w.

[13] J. Darga, J. Lamb, A. Manthiram, Industrialization of Layered Oxide Cathodes for Lithium-Ion and Sodium-Ion Batteries: A Comparative Perspective, Energy Technol. 8(12) (2020) 2000723. https://doi.org/10.1002/ente.202000723.

[14] M. Chen, Q. Liu, S.-W. Wang, E. Wang, X. Guo, S.-L. Chou, High-Abundance and Low-Cost Metal-Based Cathode Materials for Sodium-Ion Batteries: Problems, Progress, and Key Technologies, Adv. Energy Mater. 9(14) (2019) 1803609. https://doi.org/10.1002/aenm.201803609.

[15] W.-J. Li, C. Han, W. Wang, F. Gebert, S.-L. Chou, H.-K. Liu, X. Zhang, S.-X. Dou, Commercial Prospects of Existing Cathode Materials for Sodium Ion Storage, Adv. Energy Mater. 7(24) (2017) 1700274. https://doi.org/10.1002/aenm.201700274.

[16] C. Delmas, C. Fouassier, P. Hagenmuller, Structural classification and properties of the layered oxides, Physica B+C 99(1) (1980) 81-85. https://doi.org/10.1016/0378-4363(80)90214-4.

[17] W. Zuo, X. Liu, J. Qiu, D. Zhang, Z. Xiao, J. Xie, F. Ren, J. Wang, Y. Li, G.F. Ortiz, W. Wen, S. Wu, M.-S. Wang, R. Fu, Y. Yang, Engineering Na^+-layer spacings to stabilize Mn-based layered cathodes for sodium-ion batteries, Nat. Commun 12(1) (2021) 4903. https://doi.org/10.1038/s41467-021-25074-9.

[18] Q.-C. Wang, Z. Shadike, X.-L. Li, J. Bao, Q.-Q. Qiu, E. Hu, S.-M. Bak, X. Xiao, L. Ma, X.-J. Wu, X.-Q. Yang, Y.-N. Zhou, Tuning Sodium Occupancy Sites in P2-Layered Cathode

Material for Enhancing Electrochemical Performance, Adv. Energy Mater. 11(13) (2021) 2003455. https://doi.org/10.1002/aenm.202003455.

[19] H.N. Vasavan, M. Badole, S. Dwivedi, D. Kumar, P. Kumar, S. Kumar, Enhanced rate performance and specific capacity in Ti-substituted P2-type layered oxide enabled by crystal structure and particle morphology modifications, Chem. Eng. J. 448 (2022) 137662. https://doi.org/10.1016/j.cej.2022.137662.

[20] R.J. Clément, P.G. Bruce, C.P. Grey, Review—Manganese-Based P2-Type Transition Metal Oxides as Sodium-Ion Battery Cathode Materials, J. Electrochem. Soc. 162(14) (2015) A2589-A2604. https://doi.org/10.1149/2.0201514jes.

[21] D. Kundu, E. Talaie, V. Duffort, L.F. Nazar, The Emerging Chemistry of Sodium Ion Batteries for Electrochemical Energy Storage, Angew. Chem. Int. Ed. 54(11) (2015) 3431-3448. https://doi.org/10.1002/anie.201410376.

[22] J. Billaud, R.J. Clément, A.R. Armstrong, J. Canales-Vázquez, P. Rozier, C.P. Grey, P.G. Bruce, β-$NaMnO_2$: A High-Performance Cathode for Sodium-Ion Batteries, J. Am. Chem. Soc. 136(49) (2014) 17243-17248. https://doi.org/10.1021/ja509704t.

[23] Y. Zhang, R. Zhang, Y. Huang, Air-Stable Na_xTMO_2 Cathodes for Sodium Storage, Front. Chem. 7 (2019). https://doi.org/10.3389/fchem.2019.00335.

[24] L. Wang, Y.-G. Sun, L.-L. Hu, J.-Y. Piao, J. Guo, A. Manthiram, J. Ma, A.-M. Cao, Copper-substituted $Na_{0.67}Ni_{0.3-x}Cu_xMn_{0.7}O_2$ cathode materials for sodium-ion batteries with suppressed P2–O2 phase transition, J. Mater. Chem. A 5(18) (2017) 8752-8761. https://doi.org/10.1039/C7TA00880E.

[25] Y. Li, Z. Yang, S. Xu, L. Mu, L. Gu, Y.-S. Hu, H. Li, L. Chen, Air-Stable Copper-Based P2-$Na_{7/9}Cu_{2/9}Fe_{1/9}Mn_{2/3}O_2$ as a New Positive Electrode Material for Sodium-Ion Batteries, Adv. Sci. 2(6) (2015) 1500031. https://doi.org/10.1002/advs.201500031.

[26] P. Ma, W. Kang, Y. Wang, D. Cao, L. Fan, D. Sun, Binary metal co-substituted P2-type $Na_{0.67}Mn_{0.7}Cu_{0.15}Ni_{0.15}O_2$ microspheres as robust cathode for high-power sodium ion battery, Appl. Surf. Sci. 529 (2020) 147105. https://doi.org/10.1016/j.apsusc.2020.147105.

[27] W. Kang, D.Y.W. Yu, P.-K. Lee, Z. Zhang, H. Bian, W. Li, T.-W. Ng, W. Zhang, C.-S. Lee, P2-Type $Na_xCu_{0.15}Ni_{0.20}Mn_{0.65}O_2$ Cathodes with High Voltage for High-Power and Long-Life Sodium-Ion Batteries, ACS Appl. Mater. Interfaces 8(46) (2016) 31661-31668. https://doi.org/10.1021/acsami.6b10841.

[28] J. Zhang, W. Wang, W. Wang, S. Wang, B. Li, Comprehensive Review of P2-Type $Na_{2/3}Ni_{1/3}Mn_{2/3}O_2$, a Potential Cathode for Practical Application of Na-Ion Batteries, ACS Appl. Mater. Interfaces 11(25) (2019) 22051-22066. https://doi.org/10.1021/acsami.9b03937.

[29] B. Peng, Z. Sun, L. Zhao, J. Li, G. Zhang, Dual-Manipulation on P2-$Na_{0.67}Ni_{0.33}Mn_{0.67}O_2$ Layered Cathode toward Sodium-Ion Full Cell with Record Operating Voltage Beyond 3.5 V, Energy Storage Mater. 35 (2021) 620-629. https://doi.org/10.1016/j.ensm.2020.11.037.

[30] K. Wang, H. Wan, P. Yan, X. Chen, J. Fu, Z. Liu, H. Deng, F. Gao, M. Sui, Dopant Segregation Boosting High-Voltage Cyclability of Layered Cathode for Sodium Ion Batteries, Adv. Mater. 31(46) (2019) 1904816. https://doi.org/10.1002/adma.201904816.

[31] L. Yang, L.-Y. Kuo, J.M. López del Amo, P.K. Nayak, K.A. Mazzio, S. Maletti, D. Mikhailova, L. Giebeler, P. Kaghazchi, T. Rojo, P. Adelhelm, Structural Aspects of P2-Type $Na_{0.67}Mn_{0.6}Ni_{0.2}Li_{0.2}O_2$ (MNL) Stabilization by Lithium Defects as a Cathode Material for Sodium-Ion Batteries, Adv. Funct. Mater. 31(38) (2021) 2102939. https://doi.org/10.1002/adfm.202102939.

[32] Y. Xie, E. Gabriel, L. Fan, I. Hwang, X. Li, H. Zhu, Y. Ren, C. Sun, J. Pipkin, M. Dustin, M. Li, Z. Chen, E. Lee, H. Xiong, Role of Lithium Doping in P2-$Na_{0.67}Ni_{0.33}Mn_{0.67}O_2$

for Sodium-Ion Batteries, Chem. Mater. 33(12) (2021) 4445-4455. https://doi.org/10.1021/acs.chemmater.1c00569.

[33] X. Wu, G.-L. Xu, G. Zhong, Z. Gong, M.J. McDonald, S. Zheng, R. Fu, Z. Chen, K. Amine, Y. Yang, Insights into the Effects of Zinc Doping on Structural Phase Transition of P2-Type Sodium Nickel Manganese Oxide Cathodes for High-Energy Sodium Ion Batteries, ACS Appl. Mater. Interfaces 8(34) (2016) 22227-22237. https://doi.org/10.1021/acsami.6b06701.

[34] X. Wu, J. Guo, D. Wang, G. Zhong, M.J. McDonald, Y. Yang, P2-type $Na_{0.66}Ni_{0.33-x}Zn_xMn_{0.67}O_2$ as new high-voltage cathode materials for sodium-ion batteries, J. Power Sources 281 (2015) 18-26. https://doi.org/10.1016/j.jpowsour.2014.12.083.

[35] R.-M. Gao, Z.-J. Zheng, P.-F. Wang, C.-Y. Wang, H. Ye, F.-F. Cao, Recent advances and prospects of layered transition metal oxide cathodes for sodium-ion batteries, Energy Storage Mater. 30 (2020) 9-26. https://doi.org/10.1016/j.ensm.2020.04.040.

[36] Y. Li, M. Chen, B. Liu, Y. Zhang, X. Liang, X. Xia, Heteroatom Doping: An Effective Way to Boost Sodium Ion Storage, Adv. Energy Mater. 10(27) (2020) 2000927. https://doi.org/10.1002/aenm.202000927.

[37] S.-Y. Zhang, Y.-J. Guo, Y.-N. Zhou, X.-D. Zhang, Y.-B. Niu, E.-H. Wang, L.-B. Huang, P.-F. An, J. Zhang, X.-A. Yang, Y.-X. Yin, S. Xu, Y.-G. Guo, P3/O3 Integrated Layered Oxide as High-Power and Long-Life Cathode toward Na-Ion Batteries, Small 17(10) (2021) 2007236. https://doi.org/10.1002/smll.202007236.

[38] X. Liang, T.-Y. Yu, H.-H. Ryu, Y.-K. Sun, Hierarchical O3/P2 heterostructured cathode materials for advanced sodium-ion batteries, Energy Storage Mater. 47 (2022) 515-525. https://doi.org/10.1016/j.ensm.2022.02.043.

[39] K. Wang, Z.-G. Wu, G. Melinte, Z.-G. Yang, A. Sarkar, W. Hua, X. Mu, Z.-W. Yin, J.-T. Li, X.-D. Guo, B.-H. Zhong, C. Kübel, Preparation of intergrown P/O-type biphasic

layered oxides as high-performance cathodes for sodium ion batteries, J. Mater. Chem. A 9(22) (2021) 13151-13160. https://doi.org/10.1039/D1TA00627D.

[40] J.E. Wang, H. Kim, Y.H. Jung, D.K. Kim, D.J. Kim, Designing High Energy Sodium-Ion Battery Cathodes by Utilizing P2/O3 Biphasic Structure and Lithium Honeycomb Ordering, Small 17(30) (2021) 2100146. https://doi.org/10.1002/smll.202100146.

[41] C. Chen, W. Huang, Y. Li, M. Zhang, K. Nie, J. Wang, W. Zhao, R. Qi, C. Zuo, Z. Li, H. Yi, F. Pan, P2/O3 biphasic Fe/Mn-based layered oxide cathode with ultrahigh capacity and great cyclability for sodium ion batteries, Nano Energy 90 (2021) 106504. https://doi.org/10.1016/j.nanoen.2021.106504.

[42] Z. Liu, K. Jiang, S. Chu, J. Wu, H. Xu, X. Zhang, P. Wang, S. Guo, H. Zhou, Integrating P2 into O′3 toward a robust Mn-Based layered cathode for sodium-ion batteries, J. Mater. Chem. A 8(45) (2020) 23820-23826. https://doi.org/10.1039/D0TA08383F.

[43] Y. Xiao, N.M. Abbasi, Y.-F. Zhu, S. Li, S.-J. Tan, W. Ling, L. Peng, T. Yang, L. Wang, X.-D. Guo, Y.-X. Yin, H. Zhang, Y.-G. Guo, Layered Oxide Cathodes Promoted by Structure Modulation Technology for Sodium-Ion Batteries, Adv. Funct. Mater. 30(30) (2020) 2001334. https://doi.org/10.1002/adfm.202001334.

[44] B. Xiao, X. Liu, M. Song, X. Yang, F. Omenya, S. Feng, V. Sprenkle, K. Amine, G. Xu, X. Li, D. Reed, A general strategy for batch development of high-performance and cost-effective sodium layered cathodes, Nano Energy 89 (2021) 106371. https://doi.org/10.1016/j.nanoen.2021.106371.

[45] H. Su, H. Yu, Composite-Structure Materials for Na-Ion Batteries, Small Methods 3(4) (2019) 1800205. https://doi.org/10.1002/smtd.201800205.

[46] C.A. TOPAS, TOPAS-Academic: An optimization program integrating computer algebra and crystallographic objects written in C++ J, J. Appl. Crystallogr. 51 (2018) 210-218. https://doi.org/10.1107/S1600576718000183.

[47] Z. Lu, J.R. Dahn, In Situ X-Ray Diffraction Study of P2-$Na_{2/3}Ni_{1/3}Mn_{2/3}O_2$, J. Electrochem. Soc. 148(11) (2001) A1225. https://doi.org/10.1149/1.1407247.

[48] P.-F. Wang, H.-R. Yao, X.-Y. Liu, Y.-X. Yin, J.-N. Zhang, Y. Wen, X. Yu, L. Gu, Y.-G. Guo, Na^+ vacancy disordering promises high-rate Na-ion batteries, Sci. Adv. 4(3) (2018) eaar6018. https://doi.org/10.1126/sciadv.aar6018.

[49] D.H. Lee, J. Xu, Y.S. Meng, An advanced cathode for Na-ion batteries with high rate and excellent structural stability, Phys. Chem. Chem. Phys. 15(9) (2013) 3304-3312. https://doi.org/10.1039/C2CP44467D.

[50] R. Berthelot, D. Carlier, C. Delmas, Electrochemical investigation of the P2–Na_xCoO_2 phase diagram, Nat. Mater 10(1) (2011) 74-80. https://doi.org/10.1038/nmat2920.

[51] L. Wang, F. Zhou, Y.S. Meng, G. Ceder, First-principles study of surface properties of $\mathrm{Li}\mathrm{Fe}\mathrm{P}{\mathrm{O}}_{4}$: Surface energy, structure, Wulff shape, and surface redox potential, Physical Review B 76(16) (2007) 165435. https://doi.org/10.1103/PhysRevB.76.165435.

[52] H. Chung, Y. Li, M. Zhang, A. Grenier, C. Mejia, D. Cheng, B. Sayahpour, C. Song, M.H. Shen, R. Huang, E.A. Wu, K.W. Chapman, S.J. Kim, Y.S. Meng, Mitigating Anisotropic Changes in Classical Layered Oxide Materials by Controlled Twin Boundary Defects for Long Cycle Life Li-Ion Batteries, Chem. Mater. 34(16) (2022) 7302-7312. https://doi.org/10.1021/acs.chemmater.2c01234.

[53] J. Chastain, R.C. King Jr, Handbook of X-ray photoelectron spectroscopy, 1992.

[54] S. Hüfner, Photoelectron spectroscopy: principles and applications, Springer Science & Business Media2013.

[55] K. Tang, Y. Huang, X. Xie, S. Cao, L. Liu, H. Liu, Z. Luo, Y. Wang, B. Chang, H. Shu, X. Wang, Electrochemical performance and structural stability of air-stable

Na0.67Ni0.33Mn0.67-xTixO2 cathode materials for high-performance sodium-ion batteries, Chem. Eng. J. 399 (2020) 125725. https://doi.org/10.1016/j.cej.2020.125725.

[56] Q. Pei, M. Lu, Z. Liu, D. Li, X. Rao, X. Liu, S. Zhong, Improving the $Na_{0.67}Ni_{0.33}Mn_{0.67}O_2$ Cathode Material for High-Voltage Cyclability via Ti/Cu Codoping for Sodium-Ion Batteries, ACS Appl. Energy Mater. 5(2) (2022) 1953-1962. https://doi.org/10.1021/acsaem.1c03466.

[57] R. Li, Y. Liu, Z. Wang, J. Li, A P2/O3 biphasic cathode material with highly reversibility synthesized by Sn-substitution for Na-ion batteries, Electrochim. Acta 318 (2019) 14-22. https://doi.org/10.1016/j.electacta.2019.06.020.

[58] Q. Liu, Z. Hu, M. Chen, C. Zou, H. Jin, S. Wang, S.-L. Chou, S.-X. Dou, Recent Progress of Layered Transition Metal Oxide Cathodes for Sodium-Ion Batteries, Small 15(32) (2019) 1805381. https://doi.org/10.1002/smll.201805381.

[59] Z.-Y. Li, R. Gao, L. Sun, Z. Hu, X. Liu, Designing an advanced P2-$Na_{0.67}Mn_{0.65}Ni_{0.2}Co_{0.15}O_2$ layered cathode material for Na-ion batteries, J. Mater. Chem. A 3(31) (2015) 16272-16278. https://doi.org/10.1039/C5TA02450A.

[60] H. Wang, B. Yang, X.-Z. Liao, J. Xu, D. Yang, Y.-S. He, Z.-F. Ma, Electrochemical properties of P2-$Na_{2/3}[Ni_{1/3}Mn_{2/3}]O_2$ cathode material for sodium ion batteries when cycled in different voltage ranges, Electrochim. Acta 113 (2013) 200-204. https://doi.org/10.1016/j.electacta.2013.09.098.

[61] J.-H. Cheng, C.-J. Pan, J.-F. Lee, J.-M. Chen, M. Guignard, C. Delmas, D. Carlier, B.-J. Hwang, Simultaneous Reduction of Co^{3+} and Mn^{4+} in P2-$Na_{2/3}Co_{2/3}Mn_{1/3}O_2$ As Evidenced by X-ray Absorption Spectroscopy during Electrochemical Sodium Intercalation, Chem. Mater. 26(2) (2014) 1219-1225. https://doi.org/10.1021/cm403597h.

[62] A. Tripathi, A. Rudola, S.R. Gajjela, S. Xi, P. Balaya, Developing an O3 type layered oxide cathode and its application in 18650 commercial type Na-ion batteries, J. Mater. Chem. A 7(45) (2019) 25944-25960. https://doi.org/10.1039/C9TA08991H.

[63] Y. Ma, Y. Hu, Y. Pramudya, T. Diemant, Q. Wang, D. Goonetilleke, Y. Tang, B. Zhou, H. Hahn, W. Wenzel, M. Fichtner, Y. Ma, B. Breitung, T. Brezesinski, Resolving the Role of Configurational Entropy in Improving Cycling Performance of Multicomponent Hexacyanoferrate Cathodes for Sodium-Ion Batteries, Adv. Funct. Mater. 32(34) (2022) 2202372. https://doi.org/https://doi.org/10.1002/adfm.202202372.

[64] F. Wei, Q. Zhang, P. Zhang, W. Tian, K. Dai, L. Zhang, J. Mao, G. Shao, Review—Research Progress on Layered Transition Metal Oxide Cathode Materials for Sodium Ion Batteries, J. Electrochem. Soc. 168(5) (2021) 050524. https://doi.org/10.1149/1945-7111/abf9bf.

[65] J.-Y. Hwang, S.-T. Myung, Y.-K. Sun, Quaternary Transition Metal Oxide Layered Framework: O3-Type Na[Ni0.32Fe0.13Co0.15Mn0.40]O2Cathode Material for High-Performance Sodium-Ion Batteries, The Journal of Physical Chemistry C 122(25) (2018) 13500-13507. https://doi.org/10.1021/acs.jpcc.7b12140.

[66] C. Luo, A. Langrock, X. Fan, Y. Liang, C. Wang, P2-type transition metal oxides for high performance Na-ion battery cathodes, J. Mater. Chem. A 5(34) (2017) 18214-18220. https://doi.org/10.1039/c7ta04515h.

[67] Z.-Y. Li, R. Gao, J. Zhang, X. Zhang, Z. Hu, X. Liu, New insights into designing high-rate performance cathode materials for sodium ion batteries by enlarging the slab-spacing of the Na-ion diffusion layer, J. Mater. Chem. A 4(9) (2016) 3453-3461. https://doi.org/10.1039/c5ta10589g.

[68] S. Zheng, G. Zhong, M.J. McDonald, Z. Gong, R. Liu, W. Wen, C. Yang, Y. Yang, Exploring the working mechanism of Li+ in O3-type NaLi0.1Ni0.35Mn0.55O2 cathode

materials for rechargeable Na-ion batteries, J. Mater. Chem. A 4(23) (2016) 9054-9062. https://doi.org/10.1039/c6ta02230h.

[69] H.H. Sun, J.Y. Hwang, C.S. Yoon, A. Heller, C.B. Mullins, Capacity Degradation Mechanism and Cycling Stability Enhancement of AlF(3)-Coated Nanorod Gradient Na[Ni(0.65)Co(0.08)Mn(0.27)]O(2) Cathode for Sodium-Ion Batteries, ACS Nano 12(12) (2018) 12912-12922. https://doi.org/10.1021/acsnano.8b08266.

[70] T. Chen, W. Liu, F. Liu, Y. Luo, Y. Zhuo, H. Hu, J. Guo, J. Yan, K. Liu, Benefits of Copper and Magnesium Cosubstitution in Na0.5Mn0.6Ni0.4O2 as a Superior Cathode for Sodium Ion Batteries, ACS Appl. Energy Mater. 2(1) (2018) 844-851. https://doi.org/10.1021/acsaem.8b01909.

[71] Y. Ding, S. Wang, Y. Sun, Q. Liu, Q. An, H. Guo, Layered cathode-Na0.67Li0.15Ni0.18Mg0.02Mn0.8O2 with P2/O3 hybrid phase for high-performance Na-ion batteries, J. Alloys Compd. 939 (2023) 168780. https://doi.org/https://doi.org/10.1016/j.jallcom.2023.168780.

[72] J. Hong, S. Xiao, L. Deng, T. Lan, G. He, Li-free P2/O3 biphasic Na0.73Ni0.4Mn0.4Ti0.2O2 as a cathode material for sodium-ion batteries, Ionics 26(8) (2020) 3911-3917. https://doi.org/10.1007/s11581-020-03560-2.

[73] M. Bianchini, E. Gonzalo, N.E. Drewett, N. Ortiz-Vitoriano, J.M. López del Amo, F.J. Bonilla, B. Acebedo, T. Rojo, Layered P2–O3 sodium-ion cathodes derived from earth abundant elements, J. Mater. Chem. A 6(8) (2018) 3552-3559. https://doi.org/10.1039/C7TA11180K.

[74] X. Sun, X.-Y. Ji, H.-Y. Xu, C.-Y. Zhang, Y. Shao, Y. Zang, C.-H. Chen, Sodium insertion cathode material Na0.67[Ni0.4Co0.2Mn0.4]O2 with excellent electrochemical properties, Electrochim. Acta 208 (2016) 142-147. https://doi.org/https://doi.org/10.1016/j.electacta.2016.04.067.

[75] W. Weppner, R.A. Huggins, Determination of the Kinetic Parameters of Mixed-Conducting Electrodes and Application to the System Li_3Sb, J. Electrochem. Soc. 124(10) (1977) 1569. https://doi.org/10.1149/1.2133112.

[76] Q. Yang, P.-F. Wang, J.-Z. Guo, Z.-M. Chen, W.-L. Pang, K.-C. Huang, Y.-G. Guo, X.-L. Wu, J.-P. Zhang, Advanced P2-$Na_{2/3}Ni_{1/3}Mn_{7/12}Fe_{1/12}O_2$ Cathode Material with Suppressed P2–O2 Phase Transition toward High-Performance Sodium-Ion Battery, ACS Appl. Mater. Interfaces 10(40) (2018) 34272-34282. https://doi.org/10.1021/acsami.8b12204.

[77] L. Yang, S.-h. Luo, Y. Wang, Y. Zhan, Q. Wang, Y. Zhang, X. Liu, W. Mu, F. Teng, Cu-doped layered P2-type $Na_{0.67}Ni_{0.33-x}Cu_xMn_{0.67}O_2$ cathode electrode material with enhanced electrochemical performance for sodium-ion batteries, Chem. Eng. J. 404 (2021) 126578. https://doi.org/10.1016/j.cej.2020.126578.

[78] X.-H. Zhang, W.-L. Pang, F. Wan, J.-Z. Guo, H.-Y. Lü, J.-Y. Li, Y.-M. Xing, J.-P. Zhang, X.-L. Wu, P2–$Na_{2/3}Ni_{1/3}Mn_{5/9}Al_{1/9}O_2$ Microparticles as Superior Cathode Material for Sodium-Ion Batteries: Enhanced Properties and Mechanism via Graphene Connection, ACS Appl. Mater. Interfaces 8(32) (2016) 20650-20659. https://doi.org/10.1021/acsami.6b03944.

[79] L. Yu, Z. Cheng, K. Xu, Y.-X. Chang, Y.-H. Feng, D. Si, M. Liu, P.-F. Wang, S. Xu, Interlocking biphasic chemistry for high-voltage P2/O3 sodium layered oxide cathode, Energy Storage Mater. 50 (2022) 730-739. https://doi.org/10.1016/j.ensm.2022.06.012.

[Supplementary Information]

Tailored P2/O3 phase-dependent electrochemical behavior of Mn-based cathode for sodium-ion batteries

Samriddhi Saxena[a], Hari Narayanan Vasavan[a], Manish Badole[a], Asish Kumar Das[a], Sonia Deswal[b], Pradeep Kumar[b], Sunil Kumar[a], *

[a] *Department of Metallurgy Engineering and Materials Science, Indian Institute of Technology Indore, Simrol, 453552, India*

[b] *School of Physical Sciences, Indian Institute of Technology Mandi, Mandi, 175005, India*

**E-mail: sunil@iiti.ac.in*

Tables S1-S3. Crystallographic parameters of biphasic NMNC-T obtained from the Rietveld refinement of room temperature XRD data.

S1: T = 850 °C

O3 (Space Group: $R\bar{3}m$)					
Atom	**x**	**y**	**z**	**Occupancy**	**Site**
Na1	0	0	1/2	0.8	3b
Mn/Ni/Cu	0	0	0	0.6/0.3/0.1	3a
O	0	0	0.27	1	6c
P2 (Space Group: $P6_3/mmc$)					
Atom	**x**	**y**	**z**	**Occupancy**	**Site**
Na1	2/3	1/3	1/4	0.3	2d
Na2	0	0	1/4	0.5	2b
Mn/Ni/Cu	0	0	0	0.6/0.3/0.1	2a
O	2/3	1/3	0.090	1	4f

S2: T = 900 °C

O3 (Space Group: $R\bar{3}m$)					
Atom	**x**	**y**	**z**	**Occupancy**	**Site**
Na1	0	0	1/2	0.8	3b
Mn/Ni/Cu	0	0	0	0.6/0.3/0.1	3a
O	0	0	0.27	1	6c
P2 (Space Group: $P6_3/mmc$)					
Atom	**x**	**y**	**z**	**Occupancy**	**Site**
Na1	2/3	1/3	1/4	0.3	2d
Na2	0	0	1/4	0.5	2b
Mn/Ni/Cu	0	0	0	0.6/0.3/0.1	2a
O	2/3	1/3	0.092	1	4f

S3: T = 950 °C

O3 (Space Group: $R\bar{3}m$)					
Atom	**x**	**y**	**z**	**Occupancy**	**Site**
Na1	0	0	1/2	0.8	3b
Mn/Ni/Cu	0	0	0	0.6/0.3/0.1	3a
O	0	0	0.269	1	6c
P2 (Space Group: $P6_3/mmc$)					
Atom	**x**	**y**	**z**	**Occupancy**	**Site**
Na1	2/3	1/3	1/4	0.3	2d
Na2	0	0	1/4	0.5	2b
Mn/Ni/Cu	0	0	0	0.6/0.3/0.1	2a
O	2/3	1/3	0.092	1	4f

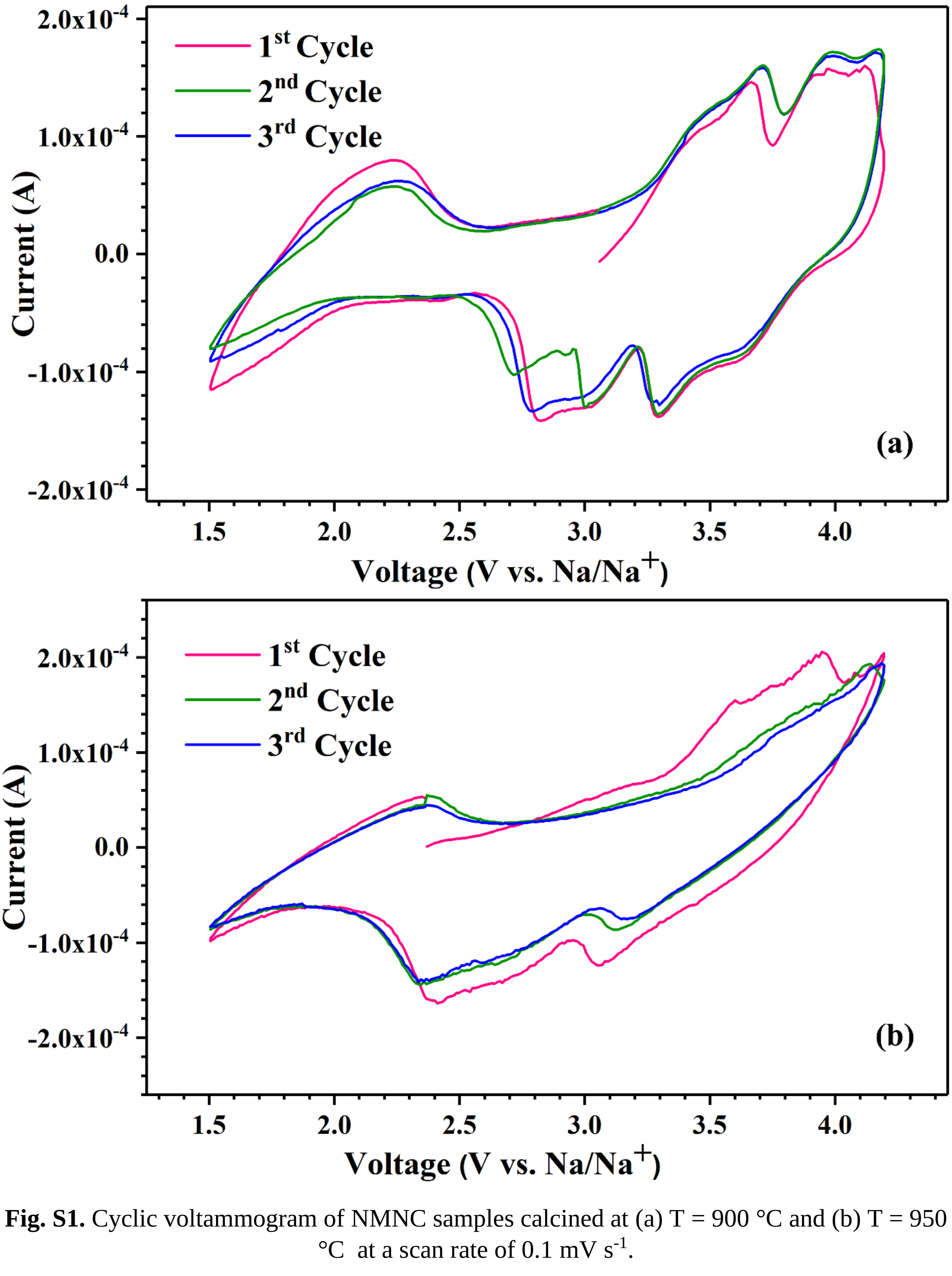

Fig. S1. Cyclic voltammogram of NMNC samples calcined at (a) T = 900 °C and (b) T = 950 °C at a scan rate of 0.1 mV s^{-1}.

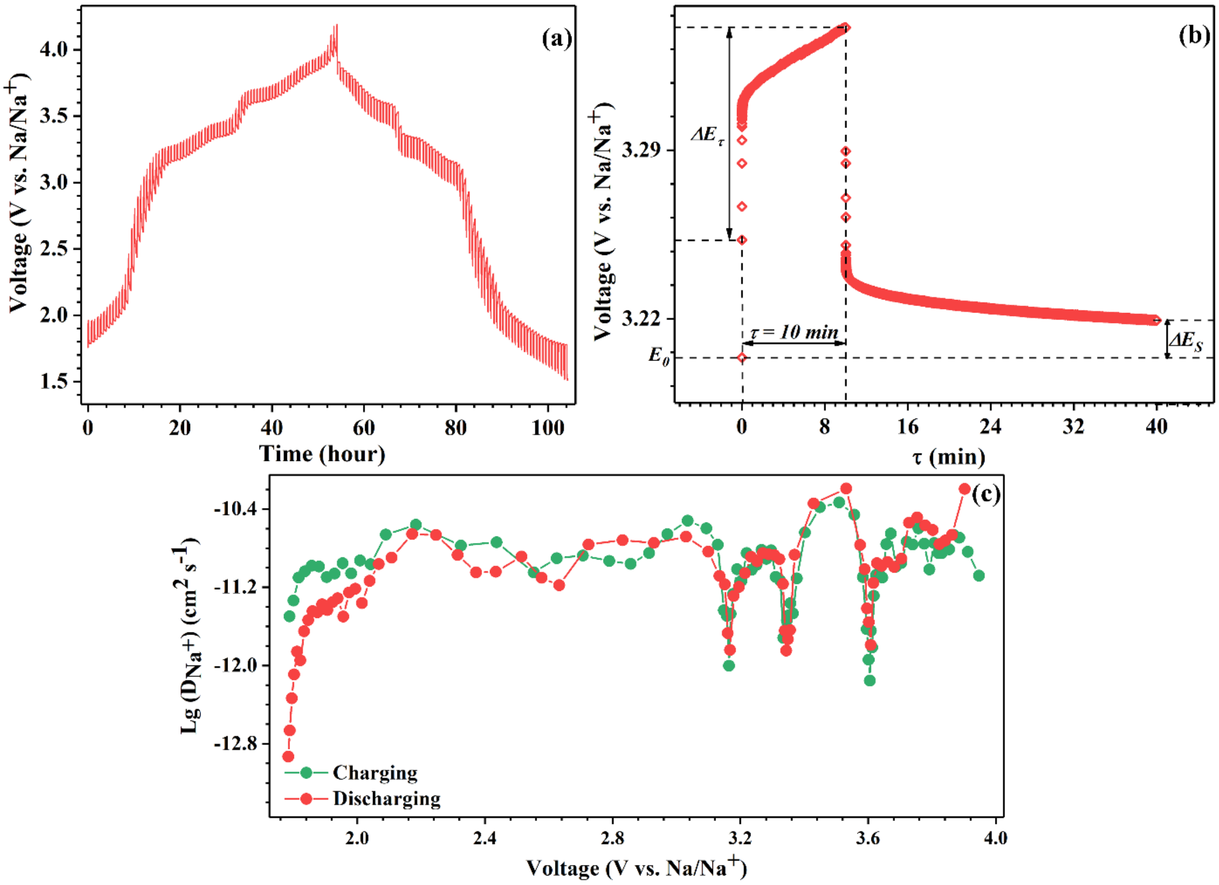

Fig. S2. (a) GITT profile of NMNC-900 cathode. (b) A single titration unit in GITT. (c) Diffusion coefficient of Na^+ at different stages during charge-discharge.

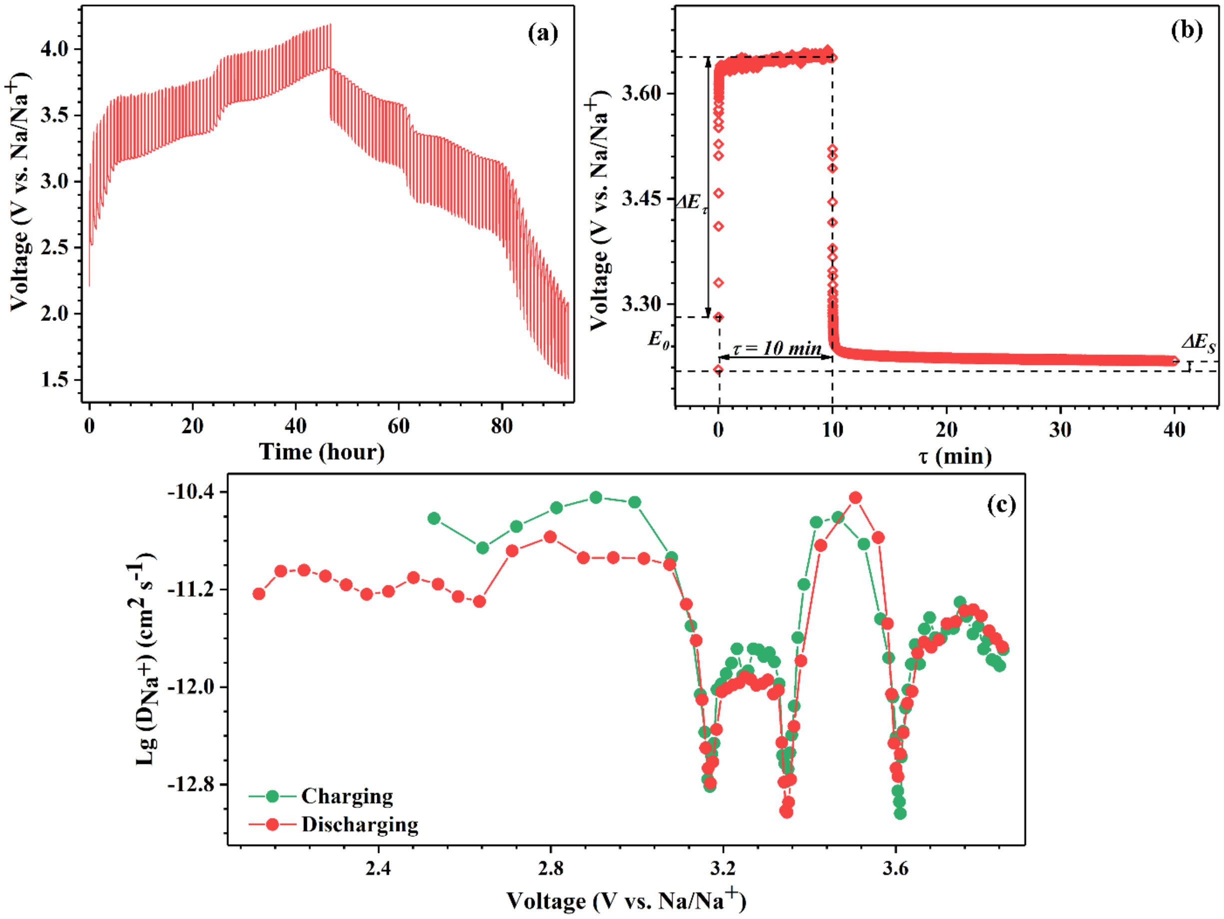

Fig. S3. (a) GITT profile of NMNC-950 cathode. (b) A single titration unit in GITT. (c) Diffusion coefficient of Na^+ at different stages during charge-discharge.

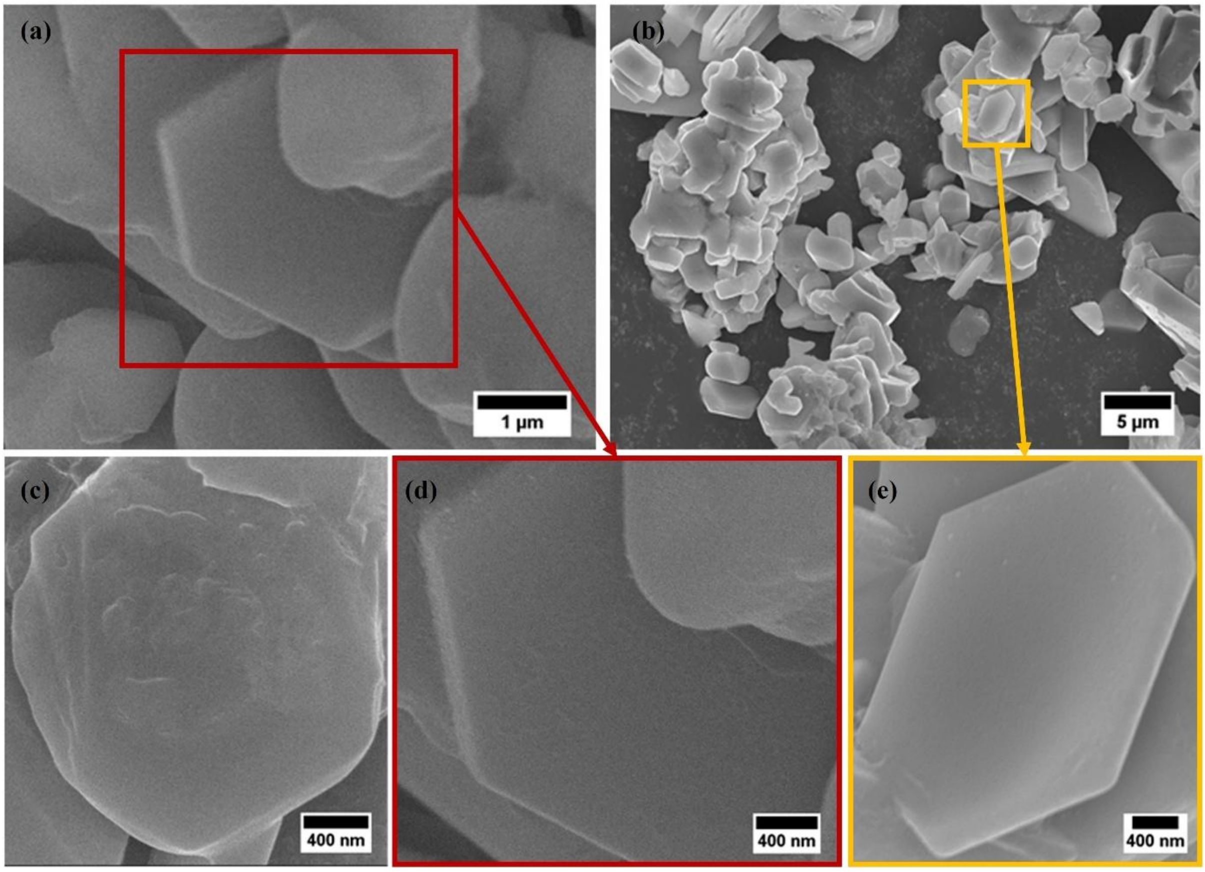

Fig. S4. SEM images of (a) NMNC-900, (b) NMNC-950, (c) NMNC-850. Figures 4(d) and 4(e) are the magnified image of 4(a) and 4(b), respectively.

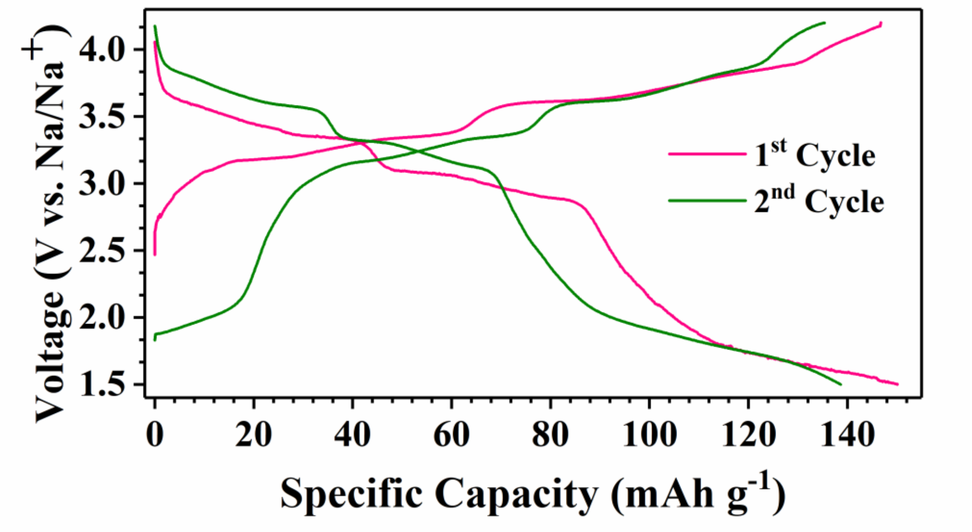

Fig. S5. First and second galvanostatic charge/discharge cycle of NMNC–850 sample at 0.1 C in a wide voltage range of 1.5-4.2 V.

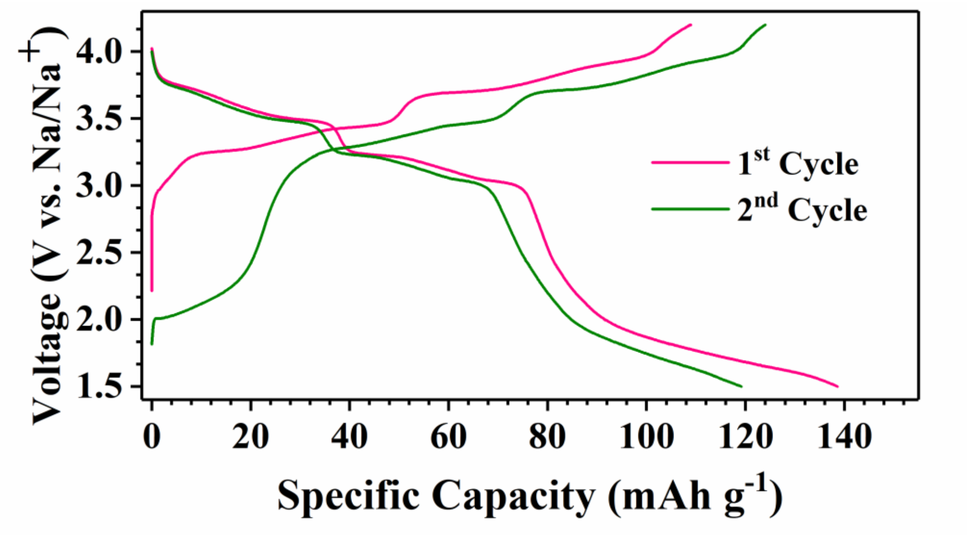

Fig. S6. First and second galvanostatic charge/discharge cycle of NMNC–900 sample at 0.1 C in a wide voltage range of 1.5-4.2 V.

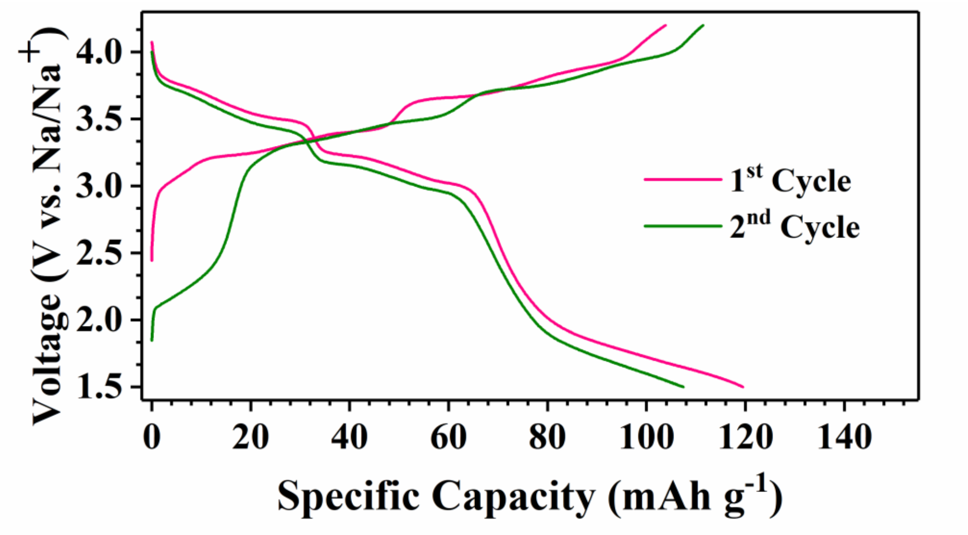

Fig. S7. First and second galvanostatic charge/discharge cycle of NMNC–950 sample at 0.1 C in a wide voltage range of 1.5-4.2 V.

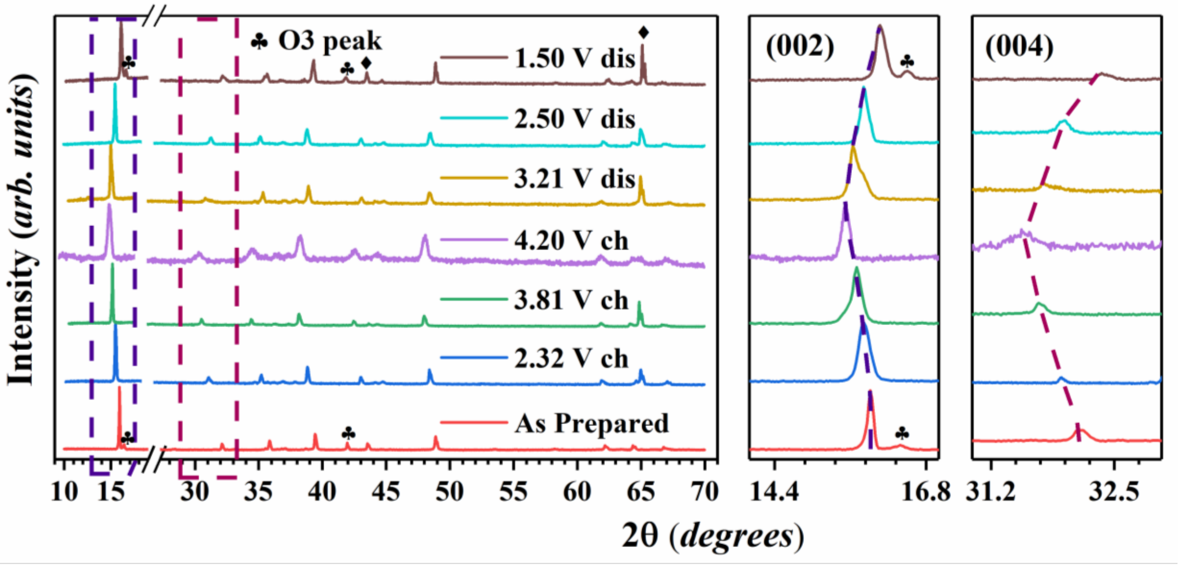

Fig. S8. Ex-situ XRD patterns of NMNC-900 sample at different states of charge between 1.5 and 4.2 V during charging (ch.) and discharging (dis.) at 0.1 C and (a1), (a2) showing the enlarged view of patterns of P2-(002) and P2-(004) peaks. The peaks denoted by ♣ represent O3 characteristic peaks returning to their initial state during discharge. The Al peaks (indicated by ◆) belong to the Al current collector.

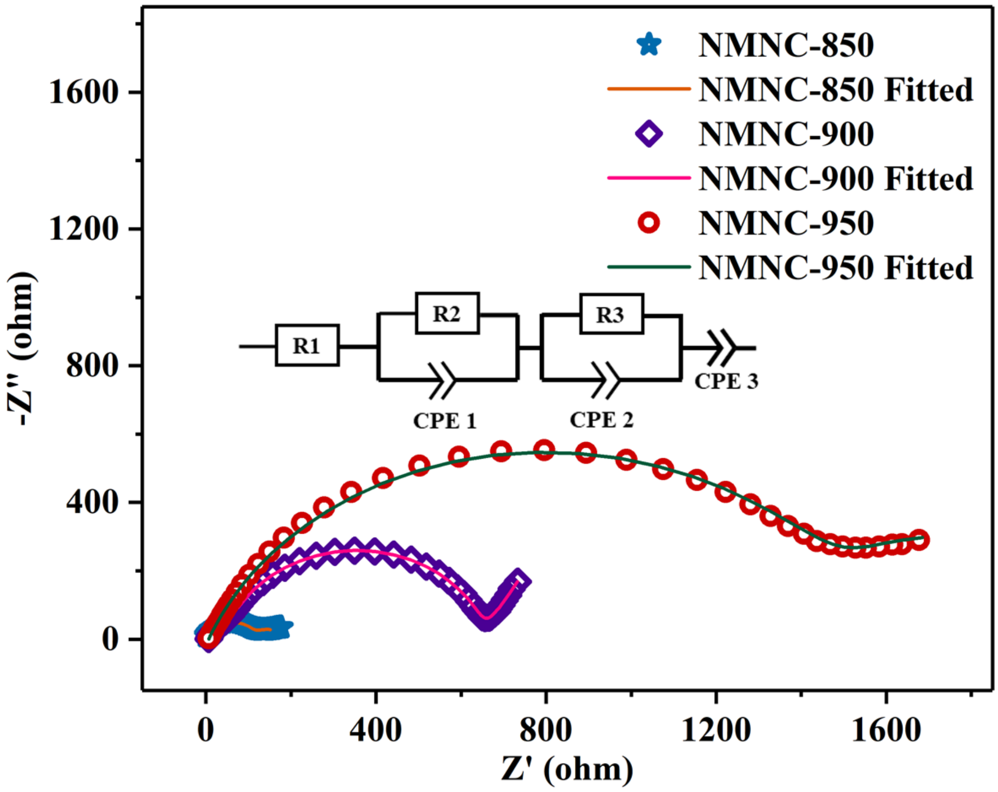

Fig. S9. The Nyquist plots along with the equivalent circuit used for fitting (solid lines) for half-cells with cathode materials calcined at various temperatures .